Robot Tracking Control with Natural Task-Space Decoupling

Alexander Dietrich, Xuwei Wu, Maged Iskandar, and Alin Albu-Schäffer

***Abstract*—There exist numerous ways to achieve multi-tasking control in kinematically redundant robots to accomplish several goals simultaneously. In all approaches, regardless of the specific type of controller, one has to make a choice about the closed-loop inertia and consequently the dynamic task couplings. Here, we introduce a new control strategy which combines two fundamentally different properties that have not been brought together yet. First, we fully dynamically decouple all individual subtasks, which cannot be achieved with classical passivity-based or hierarchical approaches. Second, we provide high robustness in practice which is structurally not possible with any inverse-dynamics approaches enforcing a decoupled but constant closed-loop inertia. Beside formal proofs of stability and passivity, we compare our approach with the other categories in various simulations and experiments. Since the proposed controller is grounded on the fundamental property of full natural task-space decoupling, this underlying strategy and its benefits can also be transferred to other design methods such as quadratic programming, MPC, or learning-based approaches.**

I. Introduction

A kinematically redundant robot such as the one illustrated in Fig. 1 is characterized by a larger number of actuated degrees of freedom (DOF) than actually necessary to perform a specific task. This redundancy makes it possible to execute additional tasks in parallel, commonly known as multi-tasking. The first works in kinematic and dynamic multi-tasking control date back to the 1980s utilizing nullspace projections to achieve a hierarchical decoupling of the subtasks [1]–[4]. In the seminal operational space formulation (OSF), linear closed-loop dynamics are enforced by the controller to decouple the task-level dynamics [4]. As investigated later in [5] one can even show that this approach and its numerous extensions such as [6]–[9] are in fact equivalent to a feedback linearization or inverse dynamics, respectively. Besides, [10] has investigated such equivalence properties, namely between projection-based dynamics and the OSF.

Over the years, multi-tasking has been addressed from several perspectives. Among others, quadratic programming (QP) has been deployed for a stack of tasks in hierarchical order which brings along the major advantage of the insertion of inequality constraints [12]–[16]. In parallel, nullspace-based approaches have been significantly advanced with the focus on high robustness in practice[1] and formal proofs of stability for safety reasons [17]–[19]. Beside the use of learning methods [20], a new track applies model predictive control (MPC) to handle multi-tasking scenarios [21]–[23].

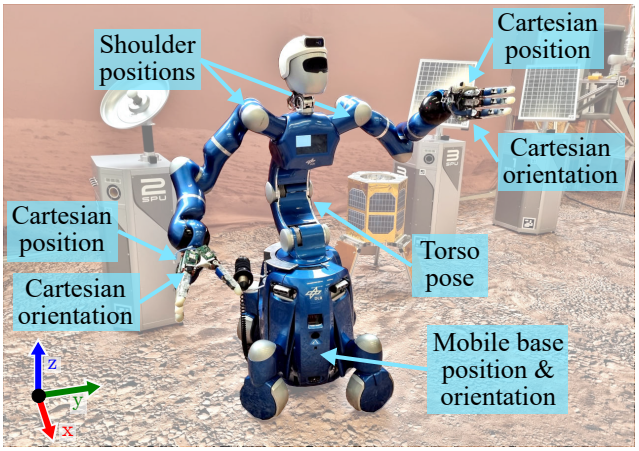

Fig. 1. Kinematically redundant humanoid robot Rollin' Justin with seven parallel control tasks. The setup in the background belongs to the Surface Avatar project [11], in which the robot has been commanded from astronauts located on the International Space Station (ISS).

Irrespective of the control strategy or approach, a deliberate choice for the closed-loop inertia has to be made in *all* cases. In order to dynamically decouple the multiple task-space dynamics, the structure of the inertia matrix has to be modified actively. Figure 2 outlines the basic categories multi-tasking controllers typically aim for. The most natural case on the left is characterized by a fully occupied matrix expressing the real, physical inertial couplings. Classical controllers such as the task-space version of PD+ control [24] or the superposition of individual subtask control actions [25]–[29] belong to this category. These controllers modify the natural dynamics as little as possible which typically leads to high robustness in practice. Moreover, they are either not affected by singularities (PD regulation controller) or they are at least less prone to stability problems when crossing singularities (PD+). However, all tasks dynamically interfere with and disturb each other. The lower triangular closed-loop

This work was supported in part by the European Research Council (ERC) through euROBIN under Grant 101070596 and by the Bavarian Ministry of Economic Affairs, Regional Development and Energy, through the project SMiLE-AI (VLR-2506-0002).

The final published version in the IEEE Transactions on Robotics is available at https://ieeexplore.ieee.org/document/11314799 with DOI: 10.1109/TRO.2025.3647777. IEEE maintains copyright of the version of record (VOR).

The authors are with the Institute of Robotics and Mechatronics, German Aerospace Center (DLR), Wessling, Germany. A. Albu-Schäffer is also with the TU Munich, Germany. Contact: alexander.dietrich@dlr.de

[1]Note that the term *robustness in practice* does not refer to a formal robustness analysis here. Rather, it refers to the intuitive notion that a controller exhibits decent control performance and stable behavior in experiments

inertia matrix in the second category comprises all hierarchical control approaches where tasks with lower priority may not disturb any higher-priority tasks. Among others, this includes concepts based on nullspace projections [30], particularly the ones ensuring dynamic consistency [4]. In recent years, the major step from multi-tasking regulation to tracking control has been taken in this research direction [17]–[19], [31], [32], the inclusion of inequality constraints has been addressed in hierarchical schemes [33], and adaption laws to manage modeling uncertainties have been proposed [34]. The structure on the right side of Fig. 2, namely the full artificial decoupling, represents the wide field of inverse dynamics and computed-torque approaches [35, p. 429]. Herein, all tasks are dynamically decoupled and constant values are enforced in the closed-loop inertia matrix. While these methods usually aim for the identity matrix as closed-loop inertia [36], one can in general also choose any other constant values instead. Full artificial decoupling is basically equivalent to feedback linearization [5] and represents the most drastic control intervention because the natural dynamics of the robot are altered to large extent. Evidently, the controlled robot will feature the best possible behavior in theory (linear closed-loop dynamics, dynamically decoupled tasks, exponential convergence) but at the cost of restrictions on the control parameter selection or severe stability issues in practice [37]. An alternative approach with full artificial decoupling has been proposed in [38]. Although the block-diagonal entries in the closed-loop inertia matrix are not constant, the choice is still artificial because configuration-dependent, physically motivated terms are introduced which do not represent the natural inertial behavior. The IDA-PBC approach [39] suggests to shape the total energy in a system, which also includes the kinetic energy involving the inertia or mass matrix, respectively. For example, the authors in [40] apply the IDA-PBC methodology to an underwater vehicle and enforce a constant diagonal mass matrix in the target dynamics which is built with the entries of the main diagonal of the original mass corresponding to a specific state.

The remaining category in Fig. 2, full natural decoupling (FND), represents the connecting link between the partial preservation of the natural dynamics and the full artificial decoupling of all subtasks, to be addressed in this paper. We will propose a control approach that manages this balancing act: fusing the practical robustness of passivity-based approaches (left side in Fig. 2) with the full dynamic decoupling of the subtasks (right side in Fig. 2). In detail, the main features and contributions of FND control are:

- The FND controller features low effective feedback gains which are comparable with passivity-based approaches such as PD+ or nullspace control. That confirms the advantages over inverse dynamics solutions in practice, which require high effective feedback gains instead.
- FND control adopts the feature of full task-space decoupling from inverse dynamics, separating the dynamic behaviors of all individual subtasks completely. That confirms the advantages over approaches such as PD+ or nullspace controllers.
- Formal proofs of stability and passivity for FND control form the theoretical basis for the application in safety-critical scenarios and human-robot interaction.
- The comparison of the proposed approach with four alternative concepts in various simulations and experiments verifies the theoretical claims and highlights the advantages over the state of the art.

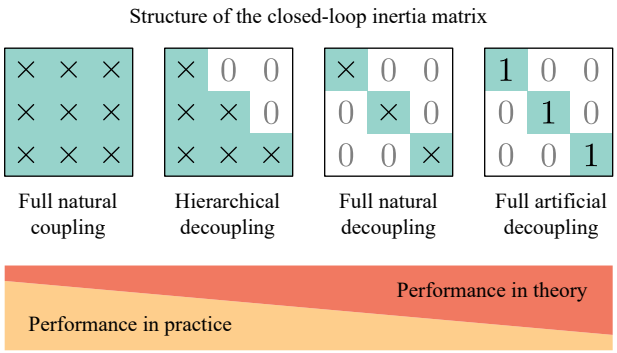

Fig. 2. Structure of the closed-loop inertia matrix. Blocks with $\times$ denote non-constant, non-zero elements. Blocks with 1 represent constant, non-zero elements.

The article is organized as follows: after the introduction of the fundamentals and notations in Section II, the controller is developed in Section III and investigated in terms of stability and passivity in Section IV. Simulations and experiments are presented in Section V and Section VI, respectively. After the discussion in Section VII, the conclusions are outlined in Section VIII.

II. Fundamentals

This section reviews the dynamics formulations and notations used in this work, taking into account the classical assumptions made.

A. Joint-Space Dynamics

The rigid-body dynamics of a robot with n actuated degrees of freedom (DOF) can be formulated as

$$\boldsymbol{M}(\boldsymbol{q})\ddot{\boldsymbol{q}} + \boldsymbol{C}(\boldsymbol{q},\dot{\boldsymbol{q}})\dot{\boldsymbol{q}} + \boldsymbol{g}(\boldsymbol{q}) = \boldsymbol{\tau} + \boldsymbol{\tau}^{\mathrm{ext}} \tag{1}$$

with $\boldsymbol{q},\dot{\boldsymbol{q}},\ddot{\boldsymbol{q}} \in \mathbb{R}^n$ representing the joint positions, velocities, and accelerations. The positive definite, symmetric term $\boldsymbol{M}(\boldsymbol{q}) \in \mathbb{R}^{n\times n}$ describes the inertia matrix, and $\boldsymbol{C}(\boldsymbol{q},\dot{\boldsymbol{q}}) \in \mathbb{R}^{n\times n}$ relates to the Coriolis/centrifugal matrix. The generalized gravity forces, control forces, and external forces are given by $\boldsymbol{g}(\boldsymbol{q}),\boldsymbol{\tau},\boldsymbol{\tau}^{\mathrm{ext}} \in \mathbb{R}^n$, respectively. The following standard assumptions are made for (1):

Assumption 1. *The quantities $\boldsymbol{M}(\boldsymbol{q})$ and $\boldsymbol{C}(\boldsymbol{q},\dot{\boldsymbol{q}})$ are uniformly bounded for all possible values of $\boldsymbol{q}$, and $\boldsymbol{C}(\boldsymbol{q},\dot{\boldsymbol{q}})$ is linear in $\dot{\boldsymbol{q}}$ [41], [42].*

Assumption 2. *The matrix $\boldsymbol{C}(\boldsymbol{q},\dot{\boldsymbol{q}})$ is formulated in a way such that $\dot{\boldsymbol{M}}(\boldsymbol{q},\dot{\boldsymbol{q}}) = \boldsymbol{C}(\boldsymbol{q},\dot{\boldsymbol{q}}) + \boldsymbol{C}(\boldsymbol{q},\dot{\boldsymbol{q}})^T$ holds and $\dot{\boldsymbol{M}}(\boldsymbol{q},\dot{\boldsymbol{q}}) - 2\boldsymbol{C}(\boldsymbol{q},\dot{\boldsymbol{q}})$ is skew-symmetric [43], [35, p. 279].*

Remark 1. *While there exist various ways to express the Coriolis and centrifugal matrix, Assumption 2 is beneficial in terms of Lyapunov-based analyses because it allows for the*

straightforward cancellation of terms related to $\dot{\boldsymbol{M}}(\boldsymbol{q},\dot{\boldsymbol{q}})$ in the time derivative of the storage function [35, p. 433].

B. Task-Space Dynamics and Task Definitions

A total number of $r \in \mathbb{N}$ independent, simultaneous tasks are defined through the task-space positions, velocities, and accelerations

$$\boldsymbol{x}_i = \boldsymbol{f}_i(\boldsymbol{q}) \ , \tag{2}$$
$$\dot{\boldsymbol{x}}_i = \boldsymbol{J}_i(\boldsymbol{q})\dot{\boldsymbol{q}} \ , \tag{3}$$
$$\ddot{\boldsymbol{x}}_i = \boldsymbol{J}_i(\boldsymbol{q})\ddot{\boldsymbol{q}} + \dot{\boldsymbol{J}}_i(\boldsymbol{q},\dot{\boldsymbol{q}})\dot{\boldsymbol{q}} \ , \tag{4}$$

for $i = 1,\dots,r$ with the dimension $m_i \in \mathbb{N}$ of the i-th task and the continuously differentiable function $\boldsymbol{f}_i(\boldsymbol{q}) : \mathbb{R}^n \to \mathbb{R}^{m_i}$. The corresponding Jacobian matrix is defined as $\boldsymbol{J}_i(\boldsymbol{q}) := \partial \boldsymbol{f}_i(\boldsymbol{q})/\partial \boldsymbol{q}$. All tasks are equally important and their total task dimension matches the dimension of the configuration space, that is, $\sum_{i=1}^{r} m_i = n$. The desired/reference task-space trajectories for these tasks depend on time t and are described by $\boldsymbol{x}_{\mathrm{d},i}(t) \in \mathbb{R}^{m_i}$ for $i = 1,\dots,r$. Their time derivatives $\dot{\boldsymbol{x}}_{\mathrm{d},i}(t)$ and $\ddot{\boldsymbol{x}}_{\mathrm{d},i}(t)$ are continuous and uniformly bounded in t. Accordingly, the task-specific errors are defined as

$$\tilde{\boldsymbol{x}}_i = \boldsymbol{x}_i - \boldsymbol{x}_{\mathrm{d},i}(t) \tag{5}$$

for $i = 1,\dots,r$ with the respective time derivatives $\dot{\tilde{\boldsymbol{x}}}_i$ and $\ddot{\tilde{\boldsymbol{x}}}_i$. To unify the notations in the following, the stacked terms

$$\boldsymbol{f}(\boldsymbol{q}) = (\boldsymbol{f}_1(\boldsymbol{q})^T,\dots,\boldsymbol{f}_r(\boldsymbol{q})^T)^T \tag{6}$$
$$\boldsymbol{x} = (\boldsymbol{x}_1^T,\dots,\boldsymbol{x}_r^T)^T \tag{7}$$
$$\boldsymbol{x}_{\mathrm{d}} = (\boldsymbol{x}_{\mathrm{d},1}^T,\dots,\boldsymbol{x}_{\mathrm{d},r}^T)^T \tag{8}$$
$$\tilde{\boldsymbol{x}} = (\tilde{\boldsymbol{x}}_1^T,\dots,\tilde{\boldsymbol{x}}_r^T)^T \tag{9}$$
$$\boldsymbol{J} = (\boldsymbol{J}_1^T,\dots,\boldsymbol{J}_r^T)^T \tag{10}$$
$$\boldsymbol{F} = (\boldsymbol{F}_1^T,\dots,\boldsymbol{F}_r^T)^T \tag{11}$$
$$\boldsymbol{F}^{\mathrm{ext}} = ((\boldsymbol{F}_1^{\mathrm{ext}})^T,\dots,(\boldsymbol{F}_r^{\mathrm{ext}})^T)^T \tag{12}$$

are introduced, where $\boldsymbol{F}$ and $\boldsymbol{F}^{\mathrm{ext}}$ contain the control inputs and external forces related to the r tasks. As $\dot{\boldsymbol{x}}$ and $\boldsymbol{F}^{\mathrm{ext}}$ are collocated and define the power port $(\dot{\boldsymbol{x}},\boldsymbol{F}^{\mathrm{ext}})$ for physical interaction with the robot in the task space, the mappings

$$\boldsymbol{\tau}^{\mathrm{ext}} = \boldsymbol{J}(\boldsymbol{q})^T\boldsymbol{F}^{\mathrm{ext}} \ , \quad \boldsymbol{\tau} = \boldsymbol{J}(\boldsymbol{q})^T\boldsymbol{F} \tag{13}$$

hold. Analogous to Section II-A, the following assumptions shall be stated:

Assumption 3. *The Jacobian matrices $\boldsymbol{J}_i(\boldsymbol{q})$ are uniformly bounded in $\boldsymbol{q}$ for all tasks $i = 1,\dots,r$ [44].*

Assumption 4. *The function $\boldsymbol{f}(\boldsymbol{q}) : \mathbb{R}^n \to \mathbb{R}^n$ is a local $\mathcal{C}^2$-diffeomorphism, and the augmented Jacobian matrix $\boldsymbol{J}(\boldsymbol{q})$ features $\mathrm{rank}(\boldsymbol{J}(\boldsymbol{q})) = n$ and is consequently invertible.*

Remark 2. *Assumption 4 implies that no singularities are crossed in the considered workspace. While this is a common assumption that is required for, e. g., many feedback-linearization-based controllers such as in most inverse dynamics approaches, it strongly depends on the proper choice of the desired task-space trajectories to avoid the singularities.*

For the sake of readability, as of now the dependencies on $\boldsymbol{q}$ and $\dot{\boldsymbol{q}}$ in the notations are omitted wherever not strictly necessary for the understanding. Combining (1)–(10), one can perform the coordinate transformation into the task space and obtain

$$\begin{aligned}\ddot{\boldsymbol{x}} + (\boldsymbol{J}\boldsymbol{M}^{-1}\boldsymbol{C} - \dot{\boldsymbol{J}})\boldsymbol{J}^{-1}\dot{\boldsymbol{x}} + \boldsymbol{J}\boldsymbol{M}^{-1}\boldsymbol{g} \\ = \boldsymbol{J}\boldsymbol{M}^{-1}(\boldsymbol{\tau} + \boldsymbol{\tau}^{\mathrm{ext}})\end{aligned} \tag{14}$$

with the fully-coupled total task-space inertia matrix

$$\boldsymbol{\Omega} = \left(\boldsymbol{J}\boldsymbol{M}^{-1}\boldsymbol{J}^T\right)^{-1} = \begin{pmatrix} \boldsymbol{\Omega}_{1,1} & \cdots & \boldsymbol{\Omega}_{1,r} \\ \vdots & \ddots & \vdots \\ \boldsymbol{\Omega}_{r,1} & \cdots & \boldsymbol{\Omega}_{r,r} \end{pmatrix} \tag{15}$$

which involves the block elements $\boldsymbol{\Omega}_{i,j} \in \mathbb{R}^{m_i \times m_j}$ for all $i = 1,\dots,r$ and $j = 1,\dots,r$. Multiplying (14) by (15) from the left yields the classical task-space dynamics

$$\boldsymbol{\Omega}\ddot{\boldsymbol{x}} + \boldsymbol{\mu}\dot{\boldsymbol{x}} + \boldsymbol{\Omega}\boldsymbol{J}\boldsymbol{M}^{-1}\boldsymbol{g} = \boldsymbol{F} + \boldsymbol{F}^{\mathrm{ext}} \tag{16}$$

with the new Coriolis and centrifugal matrix $\boldsymbol{\mu}(\boldsymbol{q},\dot{\boldsymbol{q}}) \in \mathbb{R}^{n\times n}$ featuring a similar block structure as in (15):

$$\boldsymbol{\mu} = \boldsymbol{\Omega}(\boldsymbol{J}\boldsymbol{M}^{-1}\boldsymbol{C} - \dot{\boldsymbol{J}})\boldsymbol{J}^{-1} = \begin{pmatrix} \boldsymbol{\mu}_{1,1} & \cdots & \boldsymbol{\mu}_{1,r} \\ \vdots & \ddots & \vdots \\ \boldsymbol{\mu}_{r,1} & \cdots & \boldsymbol{\mu}_{r,r} \end{pmatrix} \tag{17}$$

Due to the specific formulation of the Coriolis and centrifugal matrix according to Assumption 2, the relation

$$\dot{\boldsymbol{\Omega}} = \boldsymbol{\mu} + \boldsymbol{\mu}^T \tag{18}$$

still holds after the coordinate transformation.

III. Controller Design

The task-space dynamics (16) is naturally coupled as can be seen in the structures of $\boldsymbol{\Omega}$ and $\boldsymbol{\mu}$ in (15) and (17), respectively. Since the objective here is to dynamically decouple all r tasks, the inertia matrix has to be decoupled through active control feedback. Yet, in contrast to the classical procedure in inverse dynamics, where a feedback linearization is targeted, the desired inertia will not be set as a constant, diagonal matrix but it will be aligned with the natural term (15) as best as possible. Therefore, the desired closed-loop inertia

$$\boldsymbol{\Omega}_{\mathrm{d}} = \mathrm{diag}(\boldsymbol{\Omega}_{1,1},\dots,\boldsymbol{\Omega}_{r,r}) \ . \tag{19}$$

is specified which both conserves the natural blockdiagonal elements and decouples the r tasks. Multiplying (14) by $\boldsymbol{\Omega}_{\mathrm{d}}$ from the left yields

$$\boldsymbol{\Omega}_{\mathrm{d}}\ddot{\boldsymbol{x}} + \hat{\boldsymbol{\mu}}\dot{\boldsymbol{x}} + \boldsymbol{\Omega}_{\mathrm{d}}\boldsymbol{J}\boldsymbol{M}^{-1}\boldsymbol{g} = \boldsymbol{\Omega}_{\mathrm{d}}\boldsymbol{\Omega}^{-1}\boldsymbol{J}^{-T}(\boldsymbol{\tau} + \boldsymbol{\tau}^{\mathrm{ext}}) \tag{20}$$

with

$$\hat{\boldsymbol{\mu}} = \boldsymbol{\Omega}_{\mathrm{d}}(\boldsymbol{J}\boldsymbol{M}^{-1}\boldsymbol{C} - \dot{\boldsymbol{J}})\boldsymbol{J}^{-1} \ . \tag{21}$$

It has to be noted that the essential condition for power conservation between the time derivative of the inertia matrix

and the Coriolis/centrifugal matrix, such as represented by (18), does *not* hold for (20) anymore,[2] that is,

$$\dot{\boldsymbol{\Omega}}_{\mathrm{d}} \neq \hat{\boldsymbol{\mu}} + \hat{\boldsymbol{\mu}}^T \ . \tag{22}$$

However, one can split (17) into two parts, namely the blockdiagonal component

$$\boldsymbol{\mu}_{\mathrm{d}} = \mathrm{diag}(\boldsymbol{\mu}_{1,1}, \ldots, \boldsymbol{\mu}_{r,r}) \tag{23}$$

and the remaining outer-blockdiagonal elements contained in $\boldsymbol{\mu} - \boldsymbol{\mu}_{\mathrm{d}}$. Since $\boldsymbol{\Omega}_{\mathrm{d}}$ has been originally extracted from (15), the condition for power conservation naturally holds for $\boldsymbol{\mu}_{\mathrm{d}}$ instead of $\hat{\boldsymbol{\mu}}$:

$$\dot{\boldsymbol{\Omega}}_{\mathrm{d}} = \boldsymbol{\mu}_{\mathrm{d}} + \boldsymbol{\mu}_{\mathrm{d}}^T \ . \tag{24}$$

In other words, (24) is the reduced version of (18) which only includes the blockdiagonal components.

Based on these considerations, the following control law can be chosen:

$$\begin{aligned}\boldsymbol{\tau} = \alpha(&\boldsymbol{J}^T\boldsymbol{\Omega}\boldsymbol{\Omega}_{\mathrm{d}}^{-1}\boldsymbol{F}^{\mathrm{ext}} - \boldsymbol{\tau}^{\mathrm{ext}}) + \boldsymbol{g} \\ &+ \boldsymbol{J}^T\boldsymbol{\Omega}\boldsymbol{\Omega}_{\mathrm{d}}^{-1}\left(\hat{\boldsymbol{\mu}}\dot{\boldsymbol{x}} - \boldsymbol{\mu}_{\mathrm{d}}\dot{\boldsymbol{x}}\right) \\ &+ \boldsymbol{J}^T\boldsymbol{\Omega}\boldsymbol{\Omega}_{\mathrm{d}}^{-1}\left(\boldsymbol{\Omega}_{\mathrm{d}}\ddot{\boldsymbol{x}}_{\mathrm{d}} + \boldsymbol{\mu}_{\mathrm{d}}\dot{\boldsymbol{x}}_{\mathrm{d}} - \boldsymbol{D}\dot{\tilde{\boldsymbol{x}}} - \boldsymbol{K}\tilde{\boldsymbol{x}}\right)\end{aligned} \tag{25}$$

The binary value $\alpha \in \{0, 1\}$ enables feedback of external forces ($\alpha = 1$) or disables it ($\alpha = 0$), depending on the availability and quality of the respective measurements or estimates. Beside the compensation of gravitational effects, the control law performs a dynamics modification in the second line of (25), namely the annihilation of $\hat{\boldsymbol{\mu}}\dot{\boldsymbol{x}}$ from (20) and the introduction of $\boldsymbol{\mu}_{\mathrm{d}}\dot{\boldsymbol{x}}$ to recover the condition for power conservation stated in (24). The third line in (25) comprises the standard components of PD+ (or augmented PD) control [24]. The PD+ error feedback involves the blockdiagonal, symmetric, and positive definite stiffness and damping matrices

$$\boldsymbol{K} = \mathrm{diag}(\boldsymbol{K}_{1,1}, \ldots, \boldsymbol{K}_{r,r}) \ , \tag{26}$$

$$\boldsymbol{D}(\boldsymbol{q}) = \mathrm{diag}(\boldsymbol{D}_{1,1}(\boldsymbol{q}), \ldots, \boldsymbol{D}_{r,r}(\boldsymbol{q})) \ , \tag{27}$$

with the task-specific components $\boldsymbol{K}_{i,i}, \boldsymbol{D}_{i,i}(\boldsymbol{q}) \in \mathbb{R}^{m_i \times m_i}$ for $i = 1, \ldots, r$. The configuration dependency in the damping matrix is optional and can be used to locally realize specific damping ratios, for example. Applying (25) to (20) yields the closed-loop dynamics

$$\alpha = 0: \quad \boldsymbol{\Omega}_{\mathrm{d}}\ddot{\tilde{\boldsymbol{x}}} + (\boldsymbol{\mu}_{\mathrm{d}} + \boldsymbol{D})\dot{\tilde{\boldsymbol{x}}} + \boldsymbol{K}\tilde{\boldsymbol{x}} = \boldsymbol{\Omega}_{\mathrm{d}}\boldsymbol{\Omega}^{-1}\boldsymbol{F}^{\mathrm{ext}} \ , \tag{28}$$

$$\alpha = 1: \quad \boldsymbol{\Omega}_{\mathrm{d}}\ddot{\tilde{\boldsymbol{x}}} + (\boldsymbol{\mu}_{\mathrm{d}} + \boldsymbol{D})\dot{\tilde{\boldsymbol{x}}} + \boldsymbol{K}\tilde{\boldsymbol{x}} = \boldsymbol{F}^{\mathrm{ext}} \ . \tag{29}$$

IV. Stability and Passivity

In this section, formal proofs of exponential stability (Section IV-A) and passivity (Section IV-B) are presented and intuitively visualized (Section IV-C).

[2]Note that (20) is equivalent to (16) but just an alternative representation. Since the actual inertia and power conservation are intrinsic physical properties of the system dynamics and independent of the mathematical representation, one cannot straightforwardly extend (18) to the new formulation.

Due to the decoupled structures on the left-hand sides of (28)–(29), one can define Lyapunov candidate functions for all individual tasks $i = 1, \ldots, r$.

$$\begin{aligned}V(t, \tilde{\boldsymbol{x}}, \dot{\tilde{\boldsymbol{x}}}) &= \sum_{i=1}^{r}\left(\frac{1}{2}\dot{\tilde{\boldsymbol{x}}}_i^T\boldsymbol{\Omega}_{i,i}\dot{\tilde{\boldsymbol{x}}}_i + \frac{1}{2}\tilde{\boldsymbol{x}}_i^T\boldsymbol{K}_{i,i}\tilde{\boldsymbol{x}}_i\right) \\ &= \frac{1}{2}\begin{pmatrix}\tilde{\boldsymbol{x}} \\ \dot{\tilde{\boldsymbol{x}}}\end{pmatrix}^T\begin{pmatrix}\boldsymbol{K} & \boldsymbol{0} \\ \boldsymbol{0} & \boldsymbol{\Omega}_{\mathrm{d}}\end{pmatrix}\begin{pmatrix}\tilde{\boldsymbol{x}} \\ \dot{\tilde{\boldsymbol{x}}}\end{pmatrix}\end{aligned} \tag{30}$$

Note that the explicit time dependency in (30) originates from the change of coordinates from $(\boldsymbol{q}, \dot{\boldsymbol{q}})$ to the error states $(\tilde{\boldsymbol{x}}, \dot{\tilde{\boldsymbol{x}}})$.[3] The time derivatives can be computed as

$\underline{\alpha = 0:}$

$$\begin{aligned}\dot{V}(t, \tilde{\boldsymbol{x}}, \dot{\tilde{\boldsymbol{x}}}, \boldsymbol{F}^{\mathrm{ext}}) &= \dot{\tilde{\boldsymbol{x}}}^T\boldsymbol{\Omega}_{\mathrm{d}}\boldsymbol{\Omega}^{-1}\boldsymbol{F}^{\mathrm{ext}} - \sum_{i=1}^{r}\dot{\tilde{\boldsymbol{x}}}_i^T\boldsymbol{D}_{i,i}\dot{\tilde{\boldsymbol{x}}}_i \\ &= \dot{\tilde{\boldsymbol{x}}}^T\boldsymbol{\Omega}_{\mathrm{d}}\boldsymbol{\Omega}^{-1}\boldsymbol{F}^{\mathrm{ext}} - \begin{pmatrix}\tilde{\boldsymbol{x}} \\ \dot{\tilde{\boldsymbol{x}}}\end{pmatrix}^T\begin{pmatrix}\boldsymbol{0} & \boldsymbol{0} \\ \boldsymbol{0} & \boldsymbol{D}\end{pmatrix}\begin{pmatrix}\tilde{\boldsymbol{x}} \\ \dot{\tilde{\boldsymbol{x}}}\end{pmatrix}\end{aligned} \tag{31}$$

and

$\underline{\alpha = 1:}$

$$\begin{aligned}\dot{V}(t, \tilde{\boldsymbol{x}}, \dot{\tilde{\boldsymbol{x}}}, \boldsymbol{F}^{\mathrm{ext}}) &= \sum_{i=1}^{r}\left(\dot{\tilde{\boldsymbol{x}}}_i^T\boldsymbol{F}_i^{\mathrm{ext}} - \dot{\tilde{\boldsymbol{x}}}_i^T\boldsymbol{D}_{i,i}\dot{\tilde{\boldsymbol{x}}}_i\right) \\ &= \dot{\tilde{\boldsymbol{x}}}^T\boldsymbol{F}^{\mathrm{ext}} - \begin{pmatrix}\tilde{\boldsymbol{x}} \\ \dot{\tilde{\boldsymbol{x}}}\end{pmatrix}^T\begin{pmatrix}\boldsymbol{0} & \boldsymbol{0} \\ \boldsymbol{0} & \boldsymbol{D}\end{pmatrix}\begin{pmatrix}\tilde{\boldsymbol{x}} \\ \dot{\tilde{\boldsymbol{x}}}\end{pmatrix} \ ,\end{aligned} \tag{32}$$

inheriting the task decoupling in the damping terms in (31)–(32) and additionally in the physical interaction for $\alpha = 1$ in (32). The dependency on t and $\tilde{\boldsymbol{x}}$ arises from the configuration dependency $\boldsymbol{D}(\boldsymbol{q})$ and the subsequent change of coordinates. Since the analysis is performed in error coordinates, $\boldsymbol{D}(\boldsymbol{q})$ is expressed as $\boldsymbol{D}(t, \tilde{\boldsymbol{x}})$.

A. Proof of Stability

In the following, exponential stability is formally proven.

Proposition 1. *Consider the robot dynamics* (1) *controlled via* (25) *under the Assumptions 1–4. Then the state* $(\tilde{\boldsymbol{x}}, \dot{\tilde{\boldsymbol{x}}}) = (\boldsymbol{0}, \boldsymbol{0})$ *is uniformly exponentially stable in free motion* ($\boldsymbol{\tau}^{\mathrm{ext}} = \boldsymbol{0}$).

Remark 3. *The proof of stability is valid for both* $\alpha = 0$ *and* $\alpha = 1$ *because Proposition 1 requires* $\boldsymbol{\tau}^{\mathrm{ext}} = \boldsymbol{0}$.

Proof. Since $\boldsymbol{\Omega}_{\mathrm{d}}$ and $\boldsymbol{K}$ are symmetric and positive definite, (30) is positive definite in the error states $(\tilde{\boldsymbol{x}}, \dot{\tilde{\boldsymbol{x}}})$. For $\boldsymbol{\tau}^{\mathrm{ext}} = \boldsymbol{0}$ one can straightforwardly conclude

$$\dot{V}(t, \tilde{\boldsymbol{x}}, \dot{\tilde{\boldsymbol{x}}}) = -\dot{\tilde{\boldsymbol{x}}}^T\boldsymbol{D}\dot{\tilde{\boldsymbol{x}}} \tag{33}$$

which is, however, only negative semi-definite in $(\tilde{\boldsymbol{x}}, \dot{\tilde{\boldsymbol{x}}})$. Yet, (33) makes it possible to conclude uniform stability (US) of $(\tilde{\boldsymbol{x}}, \dot{\tilde{\boldsymbol{x}}}) = (\boldsymbol{0}, \boldsymbol{0})$ and thus boundedness of $(\tilde{\boldsymbol{x}}, \dot{\tilde{\boldsymbol{x}}})$. Since the reference trajectories $\tilde{\boldsymbol{x}}_{\mathrm{d}}, \dot{\tilde{\boldsymbol{x}}}_{\mathrm{d}}$ are bounded by definition,

[3]Under Assumption 4 one can rewrite $\boldsymbol{\Omega}_{\mathrm{d}}(\boldsymbol{q})$ as $\boldsymbol{\Omega}_{\mathrm{d}}(t, \tilde{\boldsymbol{x}})$.

see Section II-B, boundedness of $(\boldsymbol{x}, \dot{\boldsymbol{x}})$ directly follows and consequently also boundedness of $(\boldsymbol{q}, \dot{\boldsymbol{q}})$ due to Assumption 4.

In the following, the storage function (30) will be slightly modified, motivated by [43, pp. 186–187] where the level sets have been skewed. However, instead of only introducing outer-diagonal elements in (30), the auxiliary term $\epsilon^2 \boldsymbol{\Omega}_\mathrm{d}$ is added to the stiffness matrix, that is,

$$V_\epsilon(t, \tilde{\boldsymbol{x}}, \dot{\tilde{\boldsymbol{x}}}) = \frac{1}{2} \begin{pmatrix} \tilde{\boldsymbol{x}} \\ \dot{\tilde{\boldsymbol{x}}} \end{pmatrix}^T \underbrace{\begin{pmatrix} \boldsymbol{K} + \epsilon^2 \boldsymbol{\Omega}_\mathrm{d} & \epsilon \boldsymbol{\Omega}_\mathrm{d} \\ \epsilon \boldsymbol{\Omega}_\mathrm{d} & \boldsymbol{\Omega}_\mathrm{d} \end{pmatrix}}_{\boldsymbol{P}_{V_\epsilon}} \begin{pmatrix} \tilde{\boldsymbol{x}} \\ \dot{\tilde{\boldsymbol{x}}} \end{pmatrix} \ , \quad (34)$$

with the small positive constant value $\epsilon > 0$. In contrast to [43], positive definiteness of $\boldsymbol{P}_{V_\epsilon} \in \mathbb{R}^{2n \times 2n}$ becomes independent of ϵ as the Schur complement conditions show:[4]

$$\boldsymbol{\Omega}_\mathrm{d} \succ 0 \quad (35)$$

$$(\boldsymbol{K} + \epsilon^2 \boldsymbol{\Omega}_\mathrm{d}) - \epsilon^2 \boldsymbol{\Omega}_\mathrm{d} \boldsymbol{\Omega}_\mathrm{d}^{-1} \boldsymbol{\Omega}_\mathrm{d} = \boldsymbol{K} \succ 0 \quad (36)$$

The time derivative of (34) yields

$$\dot{V}_\epsilon(t, \tilde{\boldsymbol{x}}, \dot{\tilde{\boldsymbol{x}}}) = -\begin{pmatrix} \tilde{\boldsymbol{x}} \\ \dot{\tilde{\boldsymbol{x}}} \end{pmatrix}^T \underbrace{\begin{pmatrix} \epsilon \boldsymbol{K} - \frac{1}{2}\epsilon^2 \dot{\boldsymbol{\Omega}}_\mathrm{d} & \frac{1}{2}\epsilon \boldsymbol{\Psi} \\ \frac{1}{2}\epsilon \boldsymbol{\Psi}^T & \boldsymbol{D} - \epsilon \boldsymbol{\Omega}_\mathrm{d} \end{pmatrix}}_{\boldsymbol{P}_{\dot{V}_\epsilon}} \begin{pmatrix} \tilde{\boldsymbol{x}} \\ \dot{\tilde{\boldsymbol{x}}} \end{pmatrix} \quad (37)$$

with

$$\boldsymbol{\Psi} = \boldsymbol{D} - \boldsymbol{\mu}_\mathrm{d}^T - \epsilon \boldsymbol{\Omega}_\mathrm{d} \ . \quad (38)$$

In order to show negative definiteness of (37) w. r. t. $(\tilde{\boldsymbol{x}}, \dot{\tilde{\boldsymbol{x}}})$ (or positive definiteness of $\boldsymbol{P}_{\dot{V}_\epsilon}$, respectively) the Schur complement conditions

$$\epsilon \boldsymbol{K} - \tfrac{1}{2}\epsilon^2 \dot{\boldsymbol{\Omega}}_\mathrm{d} \succ 0 \quad (39)$$

$$\boldsymbol{D} - \epsilon(\boldsymbol{\Omega}_\mathrm{d} + \tfrac{1}{4}\boldsymbol{\Psi}^T (\boldsymbol{K} - \tfrac{1}{2}\epsilon \dot{\boldsymbol{\Omega}}_\mathrm{d})^{-1} \boldsymbol{\Psi}) \succ 0 \quad (40)$$

must hold. Evidently a small, positive value for ϵ exists which ensures validity of (39) as long as $\dot{\boldsymbol{\Omega}}_\mathrm{d}$ is proven bounded. Inserting (24) into (39) under Assumptions 1, 3, and 4, the required boundedness is guaranteed for bounded values of $(\boldsymbol{q}, \dot{\boldsymbol{q}})$ or $(\boldsymbol{x}, \dot{\boldsymbol{x}})$, respectively. The latter requirement has already been shown by means of US w. r. t. (33). Similarly, one can proceed to ensure validity of (40). The already established boundedness of the states can be consulted to prove boundedness of the terms $\boldsymbol{\Omega}_\mathrm{d}, \boldsymbol{\Psi}, \dot{\boldsymbol{\Omega}}_\mathrm{d}$. Consequently, a small, positive value for ϵ exists such that (40) holds. Since both (39) and (40) set requirements for $\epsilon > 0$, using the smaller value will ensure that (39)–(40) equally hold true. In consequence of that, $\boldsymbol{P}_{\dot{V}_\epsilon}$ in (37) is proven positive definite.

One can further conclude that $V_\epsilon(t, \tilde{\boldsymbol{x}}, \dot{\tilde{\boldsymbol{x}}})$ is decrescent:

$$\frac{1}{2}\underline{\lambda}(\boldsymbol{P}_{V_\epsilon}) \left|\left| \begin{pmatrix} \tilde{\boldsymbol{x}} \\ \dot{\tilde{\boldsymbol{x}}} \end{pmatrix} \right|\right|^2 \leq V_\epsilon(t, \tilde{\boldsymbol{x}}, \dot{\tilde{\boldsymbol{x}}}) \leq \frac{1}{2}\overline{\lambda}(\boldsymbol{P}_{V_\epsilon}) \left|\left| \begin{pmatrix} \tilde{\boldsymbol{x}} \\ \dot{\tilde{\boldsymbol{x}}} \end{pmatrix} \right|\right|^2 \quad (41)$$

where $\underline{\lambda}(\boldsymbol{A})$ and $\overline{\lambda}(\boldsymbol{A})$ describe the minimum and maximum eigenvalues of the matrix $\boldsymbol{A}$, respectively.

[4]Notably, this novel choice (34) for the analysis can be interpreted as a change of coordinates from $(\tilde{\boldsymbol{x}}, \dot{\tilde{\boldsymbol{x}}})$ to $(\tilde{\boldsymbol{x}}, \boldsymbol{s})$ with the sliding variable $\boldsymbol{s} = \dot{\tilde{\boldsymbol{x}}} + \epsilon \tilde{\boldsymbol{x}}$ [45]. That way, one can obtain a fully decoupled structure such as in (30) when rewriting (34) through $(\tilde{\boldsymbol{x}}, \boldsymbol{s})$ instead of $(\tilde{\boldsymbol{x}}, \dot{\tilde{\boldsymbol{x}}})$.

Now Theorem 1 from the Appendix can be applied [46]. Specifically, with $\boldsymbol{z} = (\tilde{\boldsymbol{x}}^T, \dot{\tilde{\boldsymbol{x}}}^T)^T$, $S(t, \boldsymbol{z}) = V_\epsilon(t, \tilde{\boldsymbol{x}}, \dot{\tilde{\boldsymbol{x}}})$, $\alpha_1 = \frac{1}{2}\underline{\lambda}(\boldsymbol{P}_{V_\epsilon})$, $\alpha_2 = \frac{1}{2}\overline{\lambda}(\boldsymbol{P}_{V_\epsilon})$, and $\beta = 2$, one can show (46). Since the left-hand side of (47) is given by $\dot{V}_\epsilon(t, \tilde{\boldsymbol{x}}, \dot{\tilde{\boldsymbol{x}}})$ from (37), one can choose $\alpha_3 = \underline{\lambda}(\boldsymbol{P}_{\dot{V}_\epsilon})$ such that (47) finally holds true.

Consequently, Theorem 1 enables to conclude uniform exponential stability (UES) of $(\tilde{\boldsymbol{x}}, \dot{\tilde{\boldsymbol{x}}}) = (\boldsymbol{0}, \boldsymbol{0})$ for the case of free motion ($\boldsymbol{\tau}^\mathrm{ext} = \boldsymbol{0}$) to complete the proof for Proposition 1. □

Remark 4. *As with all task-space controllers, no global stability statements are possible in general. Therefore, the extension to global UES, as mentioned in Theorem 1, cannot be made. Among others, this is due to existing singularities based on the definition of the subtasks or Cartesian tasks.*

Remark 5. *Note that ϵ is not a design parameter in the controller but it is only necessary for the analysis of the closed-loop stability. Moreover, explicit knowledge of the upper bound of ϵ is not required but merely its existence suffices to conduct the above proof for Proposition 1.*

B. Proof of Passivity

In the following, a formal proof of passivity is derived.

Proposition 2. *Consider the robot dynamics* (1) *controlled via* (25) *for $\alpha = 1$ under the Assumptions 1–4 and for the regulation case defined by $\dot{\boldsymbol{x}}_\mathrm{d} = \boldsymbol{0}$. Then the system is strictly output passive for the input $\boldsymbol{F}^\mathrm{ext}$, the output $\dot{\boldsymbol{x}}$, and the storage function* (30)*.*

Proof. The time derivative (32) with $\dot{\tilde{\boldsymbol{x}}} = \dot{\boldsymbol{x}}$ results for the storage function (30) when feedback of external forces and torques is activated ($\alpha = 1$) and the regulation case is considered. While $\dot{V}(t, \tilde{\boldsymbol{x}}, \dot{\boldsymbol{x}}, \boldsymbol{F}^\mathrm{ext})$ is only negative semi-definite in $(\tilde{\boldsymbol{x}}, \dot{\boldsymbol{x}})$, the inequality

$$\dot{V} + \underline{\lambda}(\boldsymbol{D}) \, ||\dot{\boldsymbol{x}}||^2 \leq \dot{\boldsymbol{x}}^T \boldsymbol{F}^\mathrm{ext} \quad (42)$$

holds with $\underline{\boldsymbol{\lambda}}(\boldsymbol{D}) > 0$, which is always true due to the definition of $\boldsymbol{D}$ in (27). Therefore, for the regulation case, the controlled robot dynamics (29) obtained through the application of (25) with $\alpha = 1$ to (1) lead to strict output passivity for the input $\boldsymbol{F}^\mathrm{ext}$, the output $\dot{\boldsymbol{x}}$, and the storage function V [47, Definition 2.2.8]. The power port $(\dot{\boldsymbol{x}}, \boldsymbol{F}^\mathrm{ext})$ defines the mechanical power $\dot{\boldsymbol{x}}^T \boldsymbol{F}^\mathrm{ext}$ transmitted between the robot and its environment. Hence, the respective passivity statement relates to the real power flows. □

C. Bond Graph

The power flows of the closed-loop dynamics (29) are sketched in Fig. 3 using bond graph methodology [48], [49]. The source of effort on the left-hand side injects the generalized interaction forces $\boldsymbol{F}^\mathrm{ext}$ exerted on the controlled robot by its environment. Naturally, the *virtual* power flow $\dot{\tilde{\boldsymbol{x}}}^T \boldsymbol{F}^\mathrm{ext}$ related to the depicted port is not equal to the mechanical/physical power $\dot{\boldsymbol{x}}^T \boldsymbol{F}^\mathrm{ext}$ transmitted between robot and environment during the tracking of time-dependent reference trajectories ($\dot{\boldsymbol{x}}_\mathrm{d} \neq \boldsymbol{0}$). However, when the reference trajectories

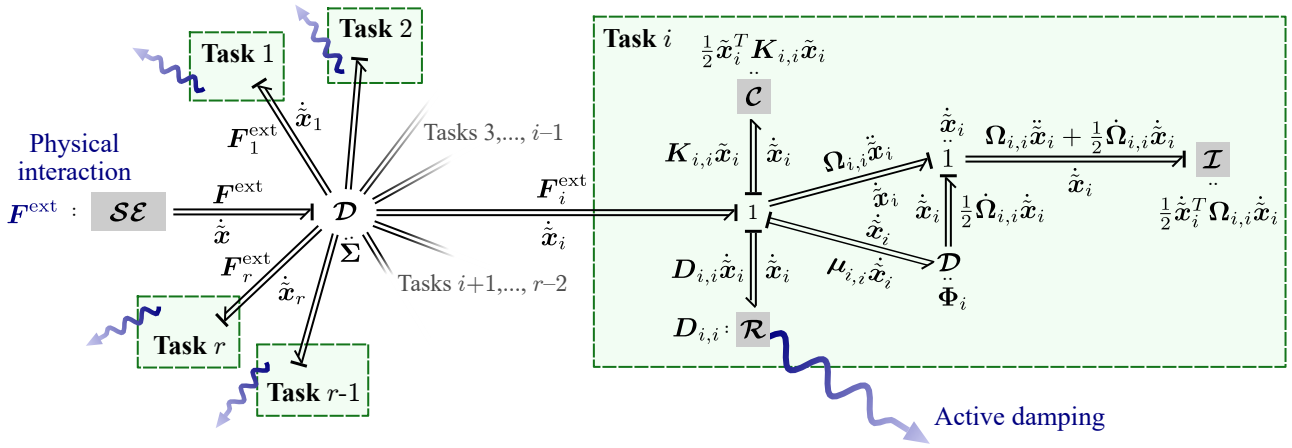

Fig. 3. Bond graph of the closed-loop system (29). The used graph elements are: capacitance ($\mathcal{C}$), inductance ($\mathcal{I}$), resistance ($\mathcal{R}$), Dirac structure ($\mathcal{D}$), 1-junction, and source of effort ($\mathcal{SE}$).

are stopped ($\dot{\boldsymbol{x}}_\mathrm{d} = \boldsymbol{0}$), the simplification $\dot{\tilde{\boldsymbol{x}}}^T \boldsymbol{F}^\mathrm{ext} = \dot{\boldsymbol{x}}^T \boldsymbol{F}^\mathrm{ext}$ holds such that Fig. 3 represents the real power flows. The Dirac structure $\boldsymbol{\Sigma}$ conserves the power following the relation

$$\begin{pmatrix} \dot{\tilde{\boldsymbol{x}}} \\ -\boldsymbol{F}_1^\mathrm{ext} \\ \vdots \\ -\boldsymbol{F}_r^\mathrm{ext} \end{pmatrix} = \begin{pmatrix} \boldsymbol{0} & \boldsymbol{I} \\ -\boldsymbol{I} & \boldsymbol{0} \end{pmatrix} \begin{pmatrix} \boldsymbol{F}^\mathrm{ext} \\ \dot{\tilde{\boldsymbol{x}}}_1 \\ \vdots \\ \dot{\tilde{\boldsymbol{x}}}_r \end{pmatrix} . \tag{43}$$

It splits $\boldsymbol{F}^\mathrm{ext}$ according to (12). As one can see in the bond graph and the respective boundaries (green/dashed boxes), the behaviors for all r tasks are decoupled. The detailed structure of each task block is exemplified by means of task i, see the particularized block on the right-hand side. Beside the modification of the energy through the ports $(\dot{\tilde{\boldsymbol{x}}}_i, \boldsymbol{F}_i^\mathrm{ext})$ for $i = 1, \ldots, r$, each block involves dissipation via active damping (27). The Dirac structure $\boldsymbol{\Phi}_i$ describes the relation

$$\begin{pmatrix} -\frac{1}{2}\dot{\boldsymbol{\Omega}}_{i,i}\dot{\tilde{\boldsymbol{x}}}_i \\ \boldsymbol{\mu}_{i,i}\dot{\tilde{\boldsymbol{x}}}_i \end{pmatrix} = \begin{pmatrix} -\frac{1}{2}(\dot{\boldsymbol{\Omega}}_{i,i} - 2\boldsymbol{\mu}_{i,i}) & -\boldsymbol{\mu}_{i,i} \\ \boldsymbol{\mu}_{i,i}^T & \dot{\boldsymbol{\Omega}}_{i,i} - 2\boldsymbol{\mu}_{i,i}^T \end{pmatrix} \begin{pmatrix} \dot{\tilde{\boldsymbol{x}}}_i \\ \dot{\tilde{\boldsymbol{x}}}_i \end{pmatrix} \tag{44}$$

for $i = 1, \ldots, r$ which is equivalent to (24).

The bond graph in Fig. 3 serves to intuitively visualize both the stability properties from Section IV-A and the proof of passivity in Section IV-B. For the condition of an undisturbed system ($\boldsymbol{\tau}^\mathrm{ext} = \boldsymbol{0}$) in the stability analysis, all power flows involving $\boldsymbol{F}^\mathrm{ext}$ and $\boldsymbol{F}_i^\mathrm{ext}$ for $i = 1, \ldots, r$ disappear. Accordingly, all task blocks in the graph are fully decoupled and isolated, which represents (28)–(29) for the case of free motion. In terms of the passivity analysis for the regulation case ($\dot{\boldsymbol{x}}_\mathrm{d} = \boldsymbol{0}$, which implies $\dot{\tilde{\boldsymbol{x}}} = \dot{\boldsymbol{x}}$) under external disturbances ($\boldsymbol{\tau}^\mathrm{ext} \neq \boldsymbol{0}$), the requirement for strict output passivity (42) can be identified by means of the power flows which cross the boundaries of the task blocks, namely through the ports $(\dot{\boldsymbol{x}}_i, \boldsymbol{F}_i^\mathrm{ext})$ for $i = 1, \ldots, r$ and the dissipation in the task-specific dampers.

D. Feedback scaling matrix

Beside control parameters such as $\boldsymbol{K}$ and $\boldsymbol{D}$ that influence the control feedback, there are further quantities which do not appear in the closed-loop dynamics (29), but they are at least as important for the closed-loop stability. The effective feedback gains involve additional terms which determine the relation between fed-back measurements/estimations (e. g., $\boldsymbol{q}, \dot{\boldsymbol{q}}, \boldsymbol{F}^\mathrm{ext}$) and the resulting, commanded joint forces and torques. Table I summarizes five different controllers which will be used in the simulations and experimental comparisons in Section V and Section VI. The third column shows the above-mentioned feedback scaling matrices. As essential components of the control laws, they significantly affect the overall system stability on the hardware. If a lower-level torque control loop, which provides the joint torque interface $\boldsymbol{\tau}$, cannot handle elements which are too high in terms of the absolute values, then instability occurs, although this effect is not visible when only looking at the closed-loop dynamics such as (29). Therefore, it is of particular interest to consider those terms and ensure that the elements do not attain excessively high values.

One can see that the task-space version of the classical PD+ controller [24] in the fourth row only involves $\boldsymbol{J}^T$, which describes the required, natural mapping from generalized task-space to generalized joint-space forces. This is due to the fact that PD+ control entirely preserves the natural inertia matrix, as already discussed on the basis of Fig. 2. If any means are taken to modify the closed-loop inertia, the feedback scaling matrix will reflect that. Examples are inverse dynamics approaches but also FND control, where the additional component $\boldsymbol{\Omega}\boldsymbol{\Omega}_\mathrm{d}^{-1}$ appears. The subsequent simulations and experiments will showcase that this term can lead to excessively high control actions and even instability, particularly if a constant desired inertia is aimed at such as in inverse dynamics approaches.

V. Simulations

The controller evaluation and the comparison with alternative approaches are conducted on a planar 6-DOF manipulator as illustrated in Fig. 4, with the depicted five individual tasks further specified in Table II. All of them are physically compatible but they feature dynamic couplings among each other as will be demonstrated in this section. The comparison

TABLE I
OVERVIEW OF THE CONTROL LAWS COMPARED IN THE SIMULATIONS, FOR THE CASE OF FREE MOTION ($\boldsymbol{\tau}^{\mathrm{ext}} = \mathbf{0}$)

Controller	Control law	Feedback scaling matrix	Implementation
FND control	$\boldsymbol{J}^T\boldsymbol{\Omega}\boldsymbol{\Omega}_{\mathrm{d}}^{-1}(\boldsymbol{\Omega}_{\mathrm{d}}\ddot{\boldsymbol{x}}_{\mathrm{d}} + \boldsymbol{\mu}_{\mathrm{d}}\dot{\boldsymbol{x}}_{\mathrm{d}} - \boldsymbol{D}\dot{\tilde{\boldsymbol{x}}} - \boldsymbol{K}\tilde{\boldsymbol{x}} + \hat{\boldsymbol{\mu}}\dot{\boldsymbol{x}} - \boldsymbol{\mu}_{\mathrm{d}}\dot{\boldsymbol{x}}) + \boldsymbol{g}$	$\boldsymbol{J}^T\boldsymbol{\Omega}\boldsymbol{\Omega}_{\mathrm{d}}^{-1}$	$\boldsymbol{\Omega}_{\mathrm{d}}$ from (19)
Inverse dynamics #1	$\boldsymbol{J}^T\boldsymbol{\Omega}\left(\ddot{\boldsymbol{x}}_{\mathrm{d}} + \hat{\boldsymbol{\mu}}\dot{\boldsymbol{x}} - \boldsymbol{D}\dot{\tilde{\boldsymbol{x}}} - \boldsymbol{K}\tilde{\boldsymbol{x}}\right) + \boldsymbol{g}$	$\boldsymbol{J}^T\boldsymbol{\Omega}$	$\boldsymbol{\Omega}_{\mathrm{d}} = \boldsymbol{I}$, [35, p. 429]
Inverse dynamics #2	$\boldsymbol{J}^T\boldsymbol{\Omega}\boldsymbol{\Omega}_{\mathrm{d}}^{-1}\left(\boldsymbol{\Omega}_{\mathrm{d}}\ddot{\boldsymbol{x}}_{\mathrm{d}} + \hat{\boldsymbol{\mu}}\dot{\boldsymbol{x}} - \boldsymbol{D}\dot{\tilde{\boldsymbol{x}}} - \boldsymbol{K}\tilde{\boldsymbol{x}}\right) + \boldsymbol{g}$	$\boldsymbol{J}^T\boldsymbol{\Omega}\boldsymbol{\Omega}_{\mathrm{d}}^{-1}$	$\boldsymbol{\Omega}_{\mathrm{d}} = \boldsymbol{\Omega}_{\mathrm{d}}(t_0)$ from (19)
PD+ control	$\boldsymbol{J}^T\left(\boldsymbol{\Omega}\ddot{\boldsymbol{x}}_{\mathrm{d}} + \boldsymbol{\mu}\dot{\boldsymbol{x}}_{\mathrm{d}} - \boldsymbol{D}\dot{\tilde{\boldsymbol{x}}} - \boldsymbol{K}\tilde{\boldsymbol{x}}\right) + \boldsymbol{g}$	$\boldsymbol{J}^T$	Task-space version of [24]
Nullspace control	$\sum_{i=1}^{r}\boldsymbol{N}_i\boldsymbol{J}_i^T\boldsymbol{F}_{i,\mathrm{ctrl}} + \boldsymbol{\tau}_{\boldsymbol{\mu}} + \boldsymbol{g}$	$\left(\boldsymbol{N}_1\boldsymbol{J}_1^T, \ldots, \boldsymbol{N}_r\boldsymbol{J}_r^T\right)$	Based on [18]

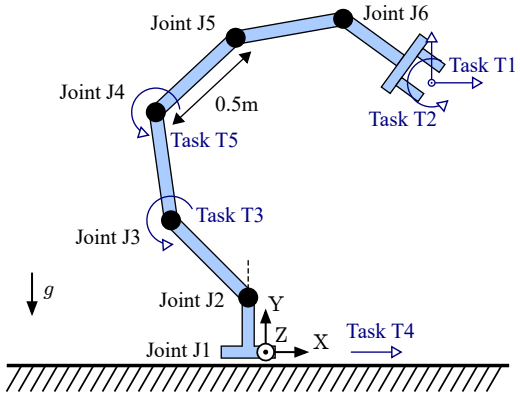

Fig. 4. Sketch of the simulation model with six DOF depicted in the initial joint configuration. Joint 1 actuates in X-direction, joints 2-6 are revolute joints. Each articulated link of 0.5 m length is described by a centered point mass of 1 kg. Joint 2 is located at a height of 0.25 m.

TABLE II
DESCRIPTION OF THE TASKS AND GAINS IN THE SIMULATIONS

Task	Description	$\boldsymbol{K}, \boldsymbol{D}$ in Sim. #1	$\boldsymbol{K}, \boldsymbol{D}$ in Sim. #2
T1	TCP in X and Y	200 $\frac{\mathrm{N}}{\mathrm{m}}$, 40 $\frac{\mathrm{Ns}}{\mathrm{m}}$	150 $\frac{\mathrm{N}}{\mathrm{m}}$, 30 $\frac{\mathrm{Ns}}{\mathrm{m}}$
T2	TCP about Z	50 $\frac{\mathrm{Nm}}{\mathrm{rad}}$, 5 $\frac{\mathrm{Nms}}{\mathrm{rad}}$	40 $\frac{\mathrm{Nm}}{\mathrm{rad}}$, 4 $\frac{\mathrm{Nms}}{\mathrm{rad}}$
T3	Joint 3	100 $\frac{\mathrm{Nm}}{\mathrm{rad}}$, 10 $\frac{\mathrm{Nms}}{\mathrm{rad}}$	80 $\frac{\mathrm{Nm}}{\mathrm{rad}}$, 8 $\frac{\mathrm{Nms}}{\mathrm{rad}}$
T4	Joint 1	300 $\frac{\mathrm{N}}{\mathrm{m}}$, 30 $\frac{\mathrm{Ns}}{\mathrm{m}}$	100 $\frac{\mathrm{N}}{\mathrm{m}}$, 10 $\frac{\mathrm{Ns}}{\mathrm{m}}$
T5	Joint 4	50 $\frac{\mathrm{Nm}}{\mathrm{rad}}$, 5 $\frac{\mathrm{Nms}}{\mathrm{rad}}$	25 $\frac{\mathrm{Nm}}{\mathrm{rad}}$, 2.5 $\frac{\mathrm{Nms}}{\mathrm{rad}}$

between the controllers includes five approaches depicted in Table I: FND control, inverse dynamics with $\boldsymbol{\Omega}_{\mathrm{d}} = \boldsymbol{I}$, inverse dynamics with the desired inertia matrix taken from (19) but being fixed at $t = t_0$, classical task-space PD+ control, and the hierarchical version of task-space PD+ control using nullspace projections with descending order of priority from task T1 down to T5.

Simulation #1 in Section V-A addresses trajectory tracking with initial task-space errors, whereas simulation #2 in Section V-B treats the regulation case or step response, respectively. Finally, Section V-C elaborates on the effective feedback gains required to implement the individual closed-loop dynamics of the five control approaches. The latter aspect relates to the quantities in the third column of Table I which pre-multiply all feedback terms such as $-\boldsymbol{K}\tilde{\boldsymbol{x}}$ or $-\boldsymbol{D}\dot{\tilde{\boldsymbol{x}}}$.

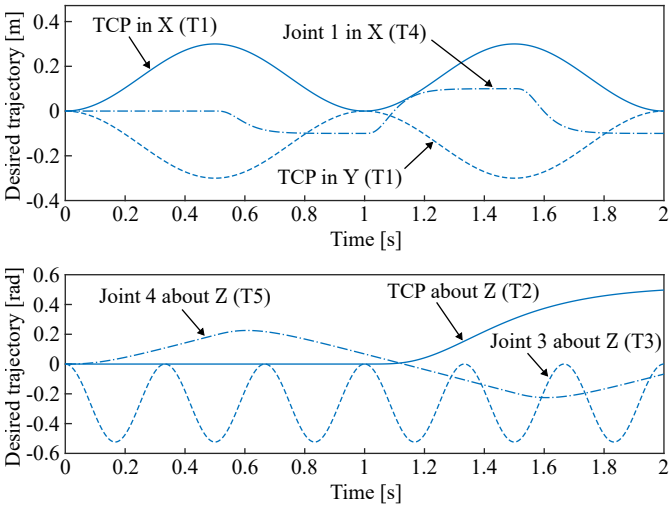

Fig. 5. Desired task-space trajectories for simulation #1. The translational tasks are displayed in the upper diagram (T1, T4), and the rotational tasks are depicted in the bottom chart (T2, T3, T5). The shown trajectories describe the time-dependent deviation from the initial desired joint configuration $[0\,\mathrm{m}, (1, -1, -1, -1, -1)\frac{1}{4}\pi\,\mathrm{rad}]^T$ at $t = 0\,\mathrm{s}$.

A. Trajectory tracking control (Simulation #1)

The tracking scenario starts with the joint configuration displayed in Fig. 4, which includes small initial task-space position errors. The time-dependent desired reference trajectories shown in Fig. 5 have to be tracked using the controller gains $\boldsymbol{K}$ and $\boldsymbol{D}$ from Table II (third column).

The storage functions for all tasks are plotted in Fig. 6 which involve the elastic potential and a velocity-error dependent term similar to (30). While all values converge to zero as expected, the charts illustrate the individual dynamic properties of the different solutions. In T1, T2, T3, and T5, one can observe the natural dynamic couplings across the task spaces in case of PD+ control. In T5, which describes the lowest priority level for the hierarchical approach, the top-down disturbance is also visible in the beginning. Interestingly, the classical inverse dynamics solution #1 with $\boldsymbol{\Omega}_{\mathrm{d}} = \boldsymbol{I}$ is partially faster (T1, T4) and partially slower (T2, T3, T5) than the other ones. This behavior can be intuitively explained by means of the natural inertia, for example, when investigating $\boldsymbol{\Omega}_{\mathrm{d}}(t_0)$.[5] In T2, the natural inertia at $t_0 = 0\,\mathrm{s}$ is about $0.41\,\mathrm{kg\,m^2}$. Since inverse

[5]Note that the natural inertia changes during trajectory tracking. Nevertheless, investigating the values at $t = t_0$ roughly indicates whether the task-specific inertias are actively scaled up or down by inverse dynamics #1.

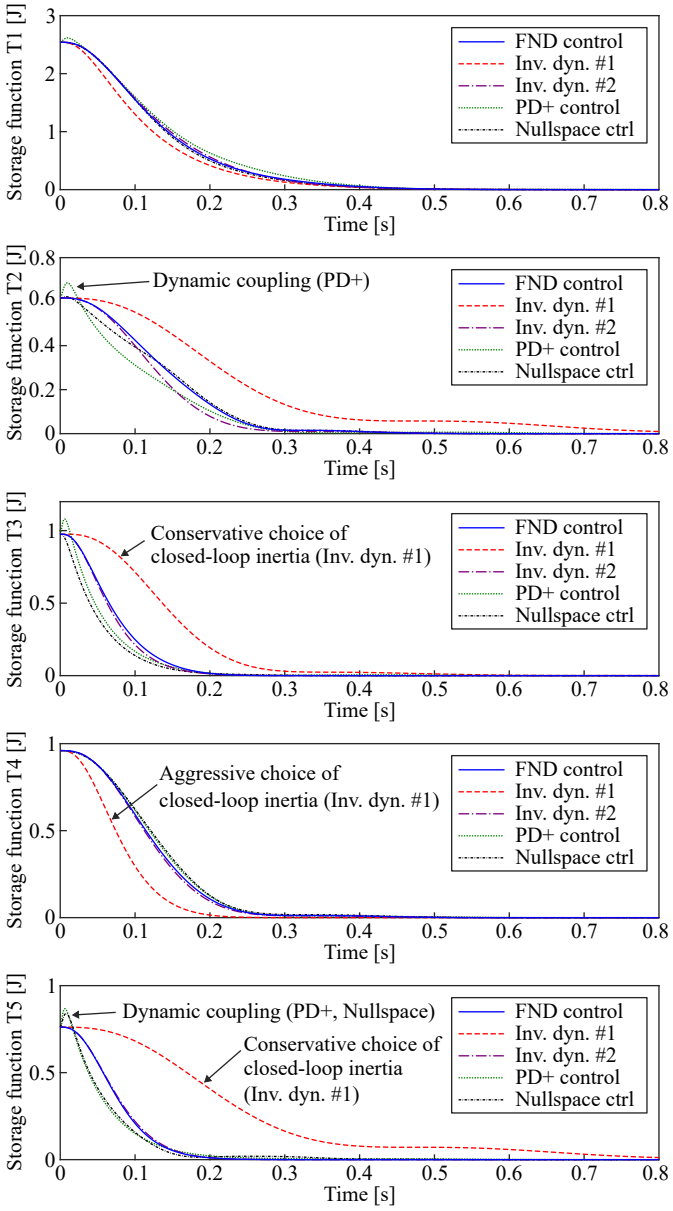

Fig. 6. Simulation #1: Storage functions for all five tasks for the tracking case with small initial task-space errors.

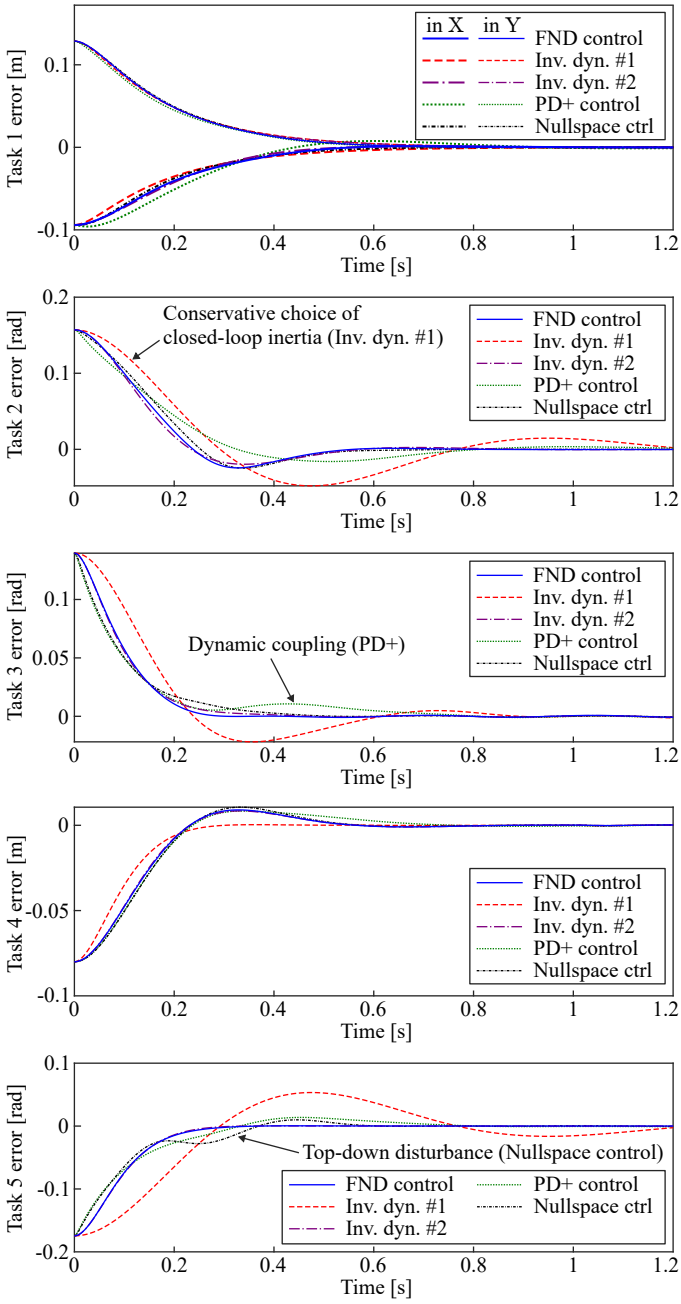

Fig. 7. Simulation #1: Tracking performance with small initial task-space errors for time-dependent, desired reference trajectories.

dynamics #1 actively enforces an inertia of $1\,\mathrm{kg\,m^2}$, this leads to a slower convergence, and the controlled system behaves overly conservative. Similarly, in T3 and T5 the natural inertias at t_0 amount to $0.22\,\mathrm{kg\,m^2}$ and $0.16\,\mathrm{kg\,m^2}$ such that the inverse dynamics #1 features inferior performance in those two tasks as well. In contrast, the convergence in T4 is superior because the natural inertia of $2.21\,\mathrm{kg}$ at t_0 is actively scaled down to $1\,\mathrm{kg}$ by the controller. The corresponding task-space errors during the tracking phase, shown in the complementary Fig. 7, consistently confirm the argumentation above. While FND control and inverse dynamics #2 feature decent and decoupled behaviors in all task spaces, the feedback scaling matrices in the controllers vary. That can be analyzed by means of the terms in the third column of Table I with the respective implementation described in the fourth column. Since they pre-multiply all feedback terms in the control laws they directly influence the effective feedback gains for the implementation of the commanded force/torque. The maximum absolute values of the matrices of dimension $n \times n$ are presented in Fig. 8.[6] As expected, PD+ control yields the lowest values due to the sole appearance of $\boldsymbol{J}^T$. Similar to the natural limitation of the scaling through the dynamically consistent nullspace projectors in the hierarchical controller, also FND control results in low values. On the contrary, both inverse dynamics solutions feature higher maximum values in general. Large values imply that the actual control parameters such as $\boldsymbol{K}$

[6]Even a single element in the $n \times n$ matrix can cause instability although the other elements might have low absolute values. Therefore, the maximum absolute values are chosen instead of the average ones or alternative metrics.

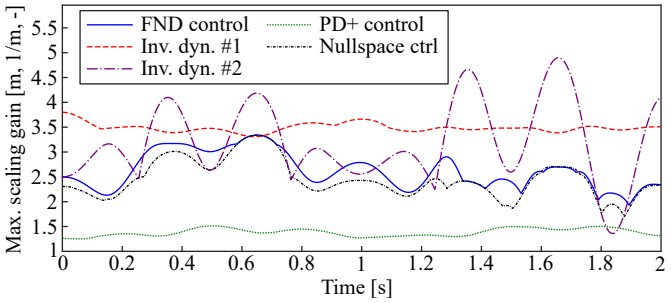

Fig. 8. Simulation #1: Maximum absolute values of the $(n \times n)$ feedback scaling matrices (third column in Table I) during trajectory tracking.

and $\boldsymbol{D}$ have to be chosen more carefully and tendentially smaller to ensure stable and safe operation when implementing the inverse dynamics controllers on real hardware. While Fig. 8 enables an initial assessment of the effective feedback gains, the considered case only represents a rather limited subset of the configuration space. Section V-C will later on examine this aspect further by means of 100,000 random joint configurations and their effect on the feedback scaling matrices, to present a more expressive analysis.

B. Regulation control (Simulation #2)

The step response is investigated using the smaller controller parameters in the fourth column of Table II due to the larger initial task-space errors: -0.17 m and -0.24 m for T1, 34° for T2, -12° for T3, -0.28 m for T4, and -25° for T5.

In Fig. 9, the respective storage functions are plotted which demonstrate the specific dynamic properties of the different control approaches similar to the tracking case. Top-down disturbances in the hierarchical control can be observed in several task spaces (T2, T5) as well as the natural dynamic couplings in classical PD+ control (T1–T5). Analogous to Section V-A, the choice $\boldsymbol{\Omega}_\mathrm{d} = \boldsymbol{I}$ for inverse dynamics #1 affects the transients, depending on the individual up- or down-scaling of the respective elements of the inertia matrix. Analogous to the tracking case, FND control and inverse dynamics #2 show a decent behavior. The maximum absolute values of the feedback scaling matrices are shown in Fig. 10. As inverse dynamics #2 enforces the initial natural inertia matrix of FND control fixed at $t = t_0$, the curves start at the same point and deviate from each other over time. However, the same trend as in simulation #1 can be observed for the five control approaches. The maximum (absolute) commanded joint forces and torques for all controllers are listed in Table III, being directly influenced by the feedback scaling matrices. One can see that high values, particularly in the joints 1 and 2 are attained for inverse dynamics #1. Indeed, this result complies with the conclusions drawn from Fig. 10. Since the largest control actions are usually commanded at the beginning of a step response, the comparable values of FND control and inverse dynamics #2 can be straightforwardly explained because the effective feedback gains of both methods are identical at $t = t_0$.

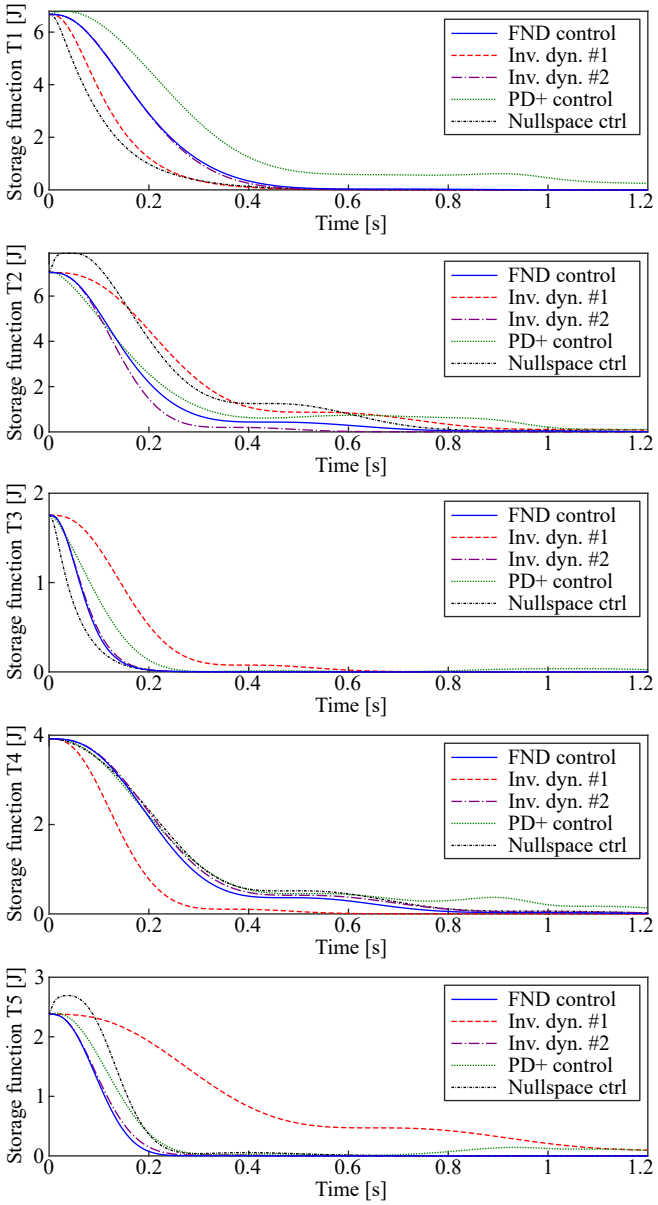

Fig. 9. Simulation #2: Storage functions for all five tasks for the regulation case with large initial task-space errors.

C. Feedback scaling matrix (Simulation #3)

The case studies in Section V-A and Section V-B indicate that inverse-dynamics-based approaches tend to scale the feedback actions to larger extent than the other methods. Yet, due to the restriction to specific joint configurations, only a small subset of the workspace has been covered so far. Here, the configuration space of the planar robot will be sampled with 100,000 random joint position values in all six joints. Although this numerical analysis does not enable a generalization, the expressiveness of the results is strengthened. Naturally there exist various singularities in the whole configuration space w. r. t. the tasks T1–T5 which no task-space controller can actually handle in its original formulation without any additional measures for singularity treatment such as [50]–[54]. Therefore, those joint configurations are excluded from the computations whose minimum singular value of the

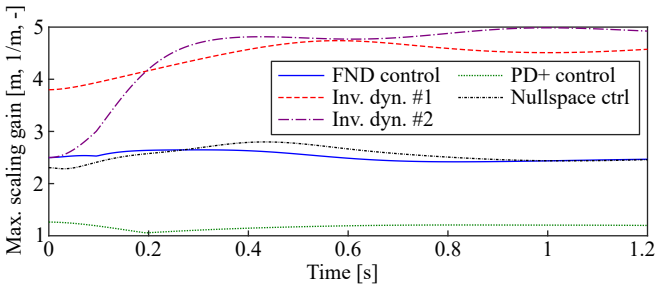

Fig. 10. Simulation #2: Maximum absolute values of the $(n \times n)$ feedback scaling matrix (third column in Table I) for the regulation case.

TABLE III
MAXIMUM ABSOLUTE JOINT FORCE AND TORQUE COMMANDS IN SIMULATION #2

	J1 [N]	J2 [Nm]	J3 [Nm]	J4 [Nm]	J5 [Nm]	J6 [Nm]
FND control	164	120	33	62	38	9
Inv. dyn. #1	**238**	**166**	54	30	37	14
Inv. dyn. #2	164	120	38	62	38	9
PD+	67	38	28	37	21	5
Nullspace control	143	102	37	53	51	26

Jacobian matrix (10) is below a given threshold. In the top chart of Fig. 11, the number of valid joint configurations is plotted against this minimum allowed singular value of $\boldsymbol{J}$, starting with a lower bound of 0.01. As the diagram reveals, the analysis starts with approximately 96.7% of the 100,000 random joint configurations (strictly speaking, 96,731). With growing threshold of the minimum allowed singular value, the number of valid configurations continuously decreases. One can summarize that the entire usable workspace of the planar manipulator is roughly covered by the depicted range up to a minimum singular value of 0.3. The second chart in Fig. 11 shows the maximum absolute values of the feedback scaling matrices. Notably, PD+, nullspace control, and FND control do not feature any problematic scaling in the whole range with maximum values of 2.5 (PD+), 6.5 (nullspace control), and 6.4 (FND control), see zoomed-in area in the center diagram. As opposed to this, both inverse dynamics solutions, which represent the active enforcement of a *constant* desired closed-loop inertia, result in high effective feedback gains. At a minimum singular value of 0.1, the maximum gains still amount to 12.5 and 31.5 although more than 66 % of the joint configurations are left. That clearly indicates that inverse-dynamics solutions, which enforce a constant inertia matrix, can potentially cause problems even in the normal workspace far away from singularities. In consequence, either the specified parameters such as $\boldsymbol{K}$ and $\boldsymbol{D}$ have to be deliberately chosen low in order to account for those effective feedback gains in inverse-dynamics methods, or the system stability is jeopardized due to the risk of excessively high feedback gains implemented in the torque control loop. This conclusion is in accord with recent studies on the consequences of active inertia shaping in order to enforce constant values in the closed-loop dynamics [37]. The bottom chart in Fig. 11 displays the median absolute values of the feedback scaling matrices

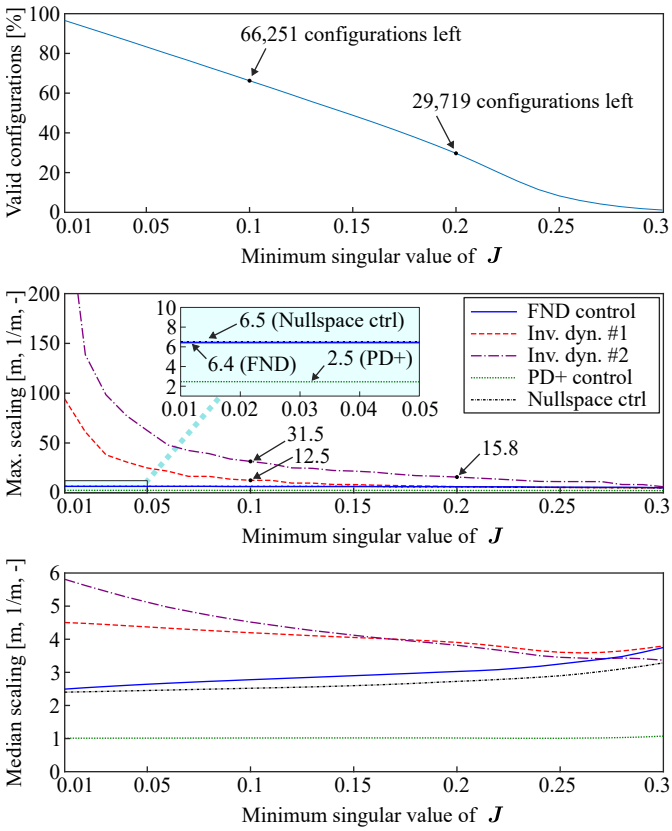

Fig. 11. Simulation #3: Analysis of the feedback scaling matrices (3rd column in Table I). With growing threshold of the minimum singular value of $\boldsymbol{J}$ and consequently larger distance to singularities, the maximum gains decrease.

which imply that not all of the n^2 elements are affected in the same way, but severe outliers cause the problem which can neither be identified nor predicted easily. Interestingly, for well-conditioned setups with minimum singular value of 0.3, FND control, inverse dynamics and hierarchical control feature median values in the range of 3–4 [m, 1/m], with continuously increasing values for the FND and hierarchical control cases up to this point. Nevertheless, these values do not appear to be problematic since the corresponding maximum absolute values stay low at the same time (center diagram). These results suggest that controllers enforcing a constant closed-loop inertia, such as inverse dynamics approaches, should be parametrized considerably more conservative due to these unpredictable, configuration-dependent effects. Consequently, these methods do not allow to effectively exploit the actual hardware capabilities of a robot.

VI. EXPERIMENTS

The experimental validation of the controller is performed on the kinematically redundant humanoid robot depicted in Fig. 1. The implemented control tasks are detailed and parametrized in Table IV. The entire task space spans all available torque-controlled DOF of the upper body. In the first experiment the tracking case is addressed, and the second one deals with the effects of external forces and torques.

TABLE IV
DESCRIPTION OF THE TASKS AND GAINS IN THE EXPERIMENTS

Task	Description	$\boldsymbol{K}, \boldsymbol{D}$ in Exp. #1	$\boldsymbol{K}, \boldsymbol{D}$ in Exp. #2
T1	Right TCP transl.	$400\,\frac{\mathrm{N}}{\mathrm{m}}$, $80\,\frac{\mathrm{Ns}}{\mathrm{m}}$	$200\,\frac{\mathrm{N}}{\mathrm{m}}$, $50\,\frac{\mathrm{Ns}}{\mathrm{m}}$
T2	Right TCP rot.	$40\,\frac{\mathrm{Nm}}{\mathrm{rad}}$, $4\,\frac{\mathrm{Nms}}{\mathrm{rad}}$	$20\,\frac{\mathrm{Nm}}{\mathrm{rad}}$, $2\,\frac{\mathrm{Nms}}{\mathrm{rad}}$
T3	Left TCP transl.	$400\,\frac{\mathrm{N}}{\mathrm{m}}$, $80\,\frac{\mathrm{Ns}}{\mathrm{m}}$	$200\,\frac{\mathrm{N}}{\mathrm{m}}$, $50\,\frac{\mathrm{Ns}}{\mathrm{m}}$
T4	Left TCP rot.	$40\,\frac{\mathrm{Nm}}{\mathrm{rad}}$, $4\,\frac{\mathrm{Nms}}{\mathrm{rad}}$	$20\,\frac{\mathrm{Nm}}{\mathrm{rad}}$, $2\,\frac{\mathrm{Nms}}{\mathrm{rad}}$
T5	Torso joints	$50\,\frac{\mathrm{Nm}}{\mathrm{rad}}$, $20\,\frac{\mathrm{Nms}}{\mathrm{rad}}$	$50\,\frac{\mathrm{Nm}}{\mathrm{rad}}$, $20\,\frac{\mathrm{Nms}}{\mathrm{rad}}$
T6	Right shoulder joint	$100\,\frac{\mathrm{Nm}}{\mathrm{rad}}$, $20\,\frac{\mathrm{Nms}}{\mathrm{rad}}$	$20\,\frac{\mathrm{Nm}}{\mathrm{rad}}$, $5\,\frac{\mathrm{Nms}}{\mathrm{rad}}$
T6	Left shoulder joint	$100\,\frac{\mathrm{Nm}}{\mathrm{rad}}$, $20\,\frac{\mathrm{Nms}}{\mathrm{rad}}$	$50\,\frac{\mathrm{Nm}}{\mathrm{rad}}$, $12\,\frac{\mathrm{Nms}}{\mathrm{rad}}$

A. Tracking control (Experiment #1)

The desired task-space trajectories are illustrated in Fig. 12, with a maximum absolute translational velocity at the right TCP of about 1 m/s. Initial errors are intentionally introduced at the right TCP and at the right shoulder. All task tracking errors, represented using Euclidean norm, are plotted in Fig. 13. Since inverse dynamics #1 leads to instability right at the start of the experiment, the emergency stop is triggered at $t \approx 0.15\,\mathrm{s}$. As one can observe, all of the remaining controllers lead to a decent performance.[7] However, inverse dynamics #2 is tendentially inferior as can be observed particularly in the right and left TCP behaviors, both in terms of translation and rotation. As discussed before, the strict enforcement of a constant desired inertia matrix in feedback-linearization-based approaches facilitates instability (inverse dynamics #1) or overly conservative control behavior (inverse dynamics #2). Since experiment #1 describes the case of undisturbed tracking, it is not surprising that the classical PD+ control performs quite well, which confirms previous analyses for joint-space control such as [37]. The reason that FND control does not clearly outperform PD+ and nullspace control might lie in the fact that the dynamic model of the robot is too imprecise to leverage the theoretical advantages of FND control here. Aside from that, the used hardware does not enable more dynamic motions than the ones shown in Fig. 12. A more modern robot could allow faster movements and consequently make the effects of undesired task-space interference more dominant in the case of PD+ control. Furthermore, more modern humanoid robots would typically feature more hip DOF with larger motion range. That would introduce distinct inertial couplings between the arms which PD+ would not be able to handle properly, in contrast to FND control. Despite the large initial errors, no significant dynamic couplings are observed in case of PD+. The coupling effects may be suppressed by joint friction on the real robot, which is not considered in the simulations presented in Section V.

B. Interaction control (Experiment #2)

In order to provide fair and reproducible conditions for the comparison under $\boldsymbol{F}^{\mathrm{ext}} \neq \boldsymbol{0}$, artificial external forces and torques are applied at the right TCP and the right shoulder joint, respectively, by means of feedforward actions superimposing the nominal torques of the respective control laws. A slow up-and-down reference trajectory is assigned to the right TCP translational task, while all other tasks should maintain their initial states. Moreover, those controllers which require feedback of $\boldsymbol{F}^{\mathrm{ext}}$ to generate the control action do not have direct access to these quantities but only to their estimations obtained through a common momentum-based disturbance observer [55], [56]. The first two diagrams in Fig. 14 show the applied disturbances and their estimations used in the control laws. Since the hierarchical null space based controller [18] can also be implemented using feedback of external forces and torques, both versions are shown in the following for the sake of completeness. The lower four diagrams in Fig. 14 depict the relevant task-space errors.[8] For the right TCP translational task and the right shoulder task, which involve artificial interactions, the difference between the actual task errors and the expected deviations is shown instead of task errors. The expected deviation is computed via the artificial external forces/torques $\boldsymbol{F}^{\mathrm{ext}}_{\mathrm{art},i}$ and contact stiffness, based on the desired impedance in the quasi-static case ($\dot{\tilde{\boldsymbol{x}}} = \ddot{\tilde{\boldsymbol{x}}} = \boldsymbol{0}$), as $\boldsymbol{K}_i^{-1}\boldsymbol{F}^{\mathrm{ext}}_{\mathrm{art},i}$. This evaluation is justified by the slow reference trajectory of the right TCP translational task. Note that inverse dynamics #1 is not presented in the diagrams because severe instability occurs immediately after the controller is switched on. The blue-shaded areas highlight the regions in which there should be ideally zero errors. These areas refer to task spaces in which no external force or torque is applied. The plots clearly reveal that any controller omitting feedback of external

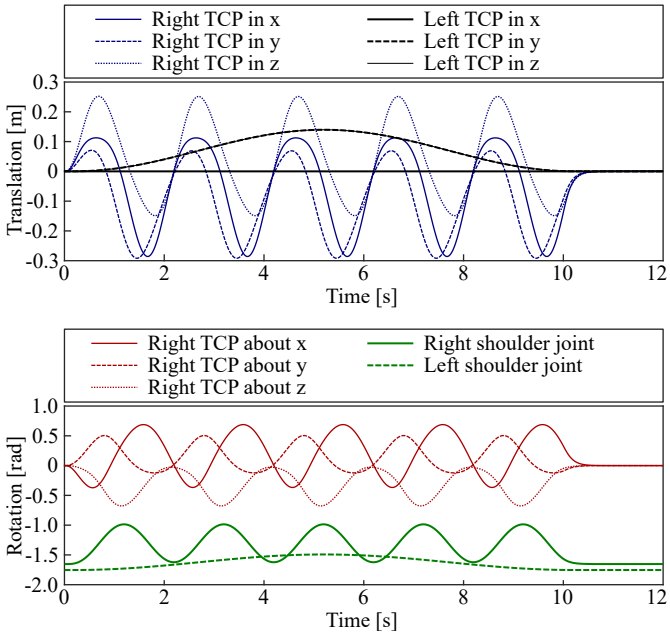

Fig. 12. Experiment #1: Desired trajectories for the subtasks. The curves related to all TCP motions describe the deviations from the initial positions and orientations, respectively. The desired orientation at the right TCP is described by the Euler angles of type x-y-z.

[7]Note that the comparatively low stiffness gains in Table IV result in a compliant behavior, which can be observed in non-negligible steady-state errors (e. g., almost 0.1 rad Euclidean norm for torso joints). Such a behavior is expected for impedance-based control.

[8]The task-space errors related to the left arm are omitted. They do not feature noteworthy differences since the arms are physically decoupled to a large extent because of the limited motion/dynamic capabilities of the torso.

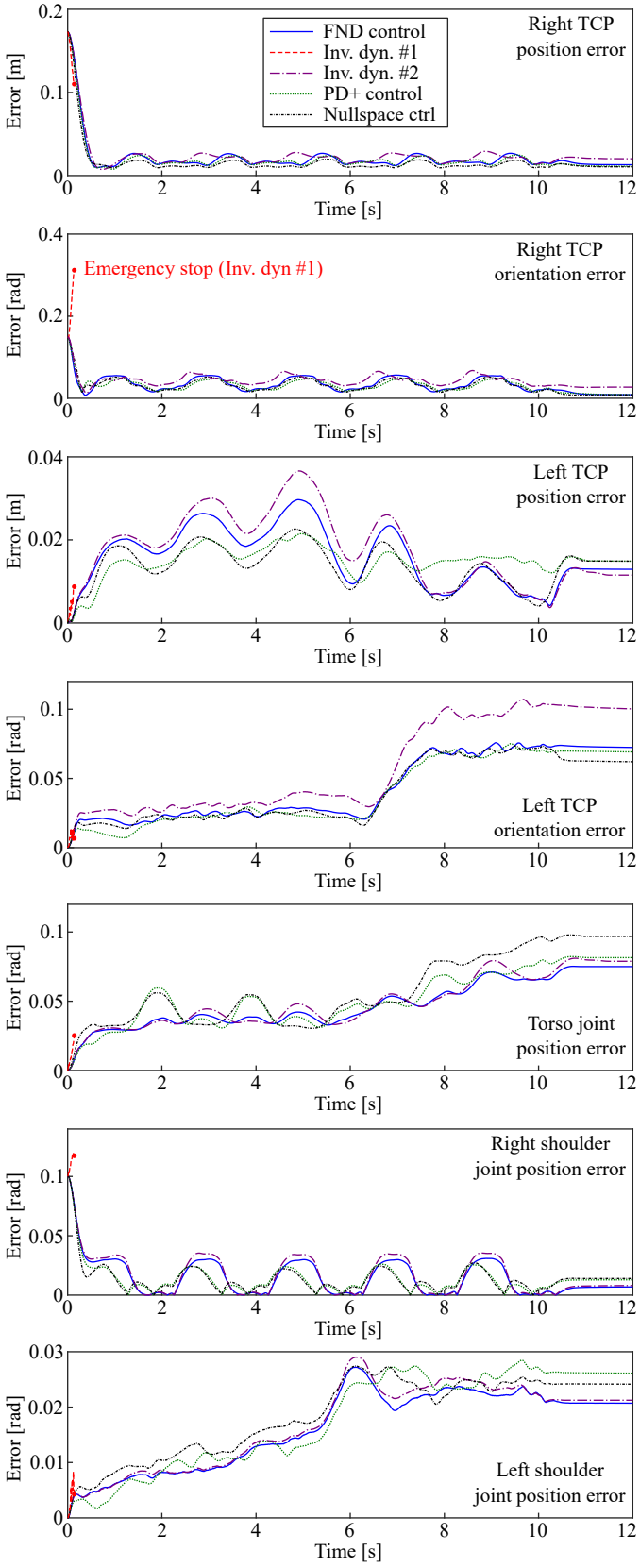

Fig. 13. Experiment #1: Tracking errors in all task spaces. Since inverse dynamics #1 destabilizes the closed-loop system, the emergency stop is triggered at $t \approx 0.15\,\mathrm{s}$.

forces and torques (PD+ control and nullspace control without feedback of $\boldsymbol{F}^{\mathrm{ext}}$) suffers from the natural couplings across the subtask dynamics related to these external interactions. Comparing the two nullspace controllers with each other also illustrates this fundamental aspect: using feedback of $\boldsymbol{F}^{\mathrm{ext}}$ results in demonstrably lower errors during interaction.

VII. Discussion

A direct comparison with reference to the fundamentally different concepts sketched in Fig. 2 is made. Table V elaborates on the various ways to treat the closed-loop inertia on the basis of the discussed approaches and strategies. While such a rating is subjective to a certain extent, the relative differences and tendencies are clear and confirm the initial claim that FND control properly manages the compromise between practice/implementation on the one side and theoretical/convergence properties on the other side. Regarding the behavior in singularities, two aspects require explanation. Firstly, a majority of control approaches experience severe stability problems when crossing singularities. This is evident when examining the control laws in Table I. Quantities like $\boldsymbol{\Omega}, \boldsymbol{\mu}, \hat{\boldsymbol{\mu}}, \boldsymbol{N}_i$ require the inversion of the Jacobian matrix, thus leading to problems when applying the control law. Therefore, all controllers have been marked with (**––**) except for PD+ control (**–**) because it does not involve a pre-multiplication by $\boldsymbol{\Omega}$ for the position and velocity error variables. Moreover, when a task-space PD controller (**+**) is used, no excessive control actions result. Although the classical PD regulation controller is unable to achieve the control goals in singular configurations as well, no instabilities occur. Secondly, in general it is possible to modify all control methods in a way such that singularity crossing becomes possible [50]–[54].

Equation (28) has revealed that a modified closed-loop inertia ($\boldsymbol{\Omega}_{\mathrm{d}} \neq \boldsymbol{\Omega}$) requires feedback of $\boldsymbol{F}^{\mathrm{ext}}$ and $\boldsymbol{\tau}^{\mathrm{ext}}$ in the controller. Otherwise, the desired stiffness $\boldsymbol{K}$ will not be perceived during physical interaction with the robot. It is well known that this limitation is problematic in inverse dynamics approaches [37]. Setting $\alpha = 1$ in (25) shows the consequences of this necessity. Beside the complete annihilation of $\boldsymbol{\tau}^{\mathrm{ext}}$, the introduction of $\boldsymbol{F}^{\mathrm{ext}}$ implies the pre-multiplication by $\boldsymbol{J}^T \boldsymbol{\Omega} \boldsymbol{\Omega}_{\mathrm{d}}^{-1}$ or by the feedback scaling matrix in Table I (third column), respectively. As a matter of fact, the same relations as already analyzed before come into play and justify that the proposed FND control does not cause problems during interaction because of small elements in the feedback scaling matrix, see Fig. 11 (second diagram). In contrast, large matrix elements (inverse dynamics #1 and #2) can potentially destabilize the controlled robot if one aims at a correct interaction stiffness $\boldsymbol{K}$ in inverse dynamics approaches, because a similar annihilation of $\boldsymbol{\tau}^{\mathrm{ext}}$ and reintroduction of $\boldsymbol{F}^{\mathrm{ext}}$ has to be implemented accordingly. This is a particularly serious issue because the signal quality of $\boldsymbol{F}^{\mathrm{ext}}$ is often poor due to identification or estimation algorithms which introduce delays and other classical observer effects. For this reason, full artificial decoupling approaches are marked with **––** in Table V regarding the feedback of $\boldsymbol{F}^{\mathrm{ext}}$. The implementation of a desired contact stiffness in

a feedback-linearized system is structurally problematic and always carries the risk of instability. This conclusion is in line with recent insights from hybrid motion-force control [57], where the authors state that it is "*preferable to choose the shaped inertia as close to the natural inertia as possible*" for the decoupling of motion- and force-subspaces, in order to reduce the amplification of disturbance forces. This discussion raises the controversial question: Why should one enforce a constant closed-loop inertia at all, if dynamic task decoupling can also be achieved through FND control while implementing considerably lower effective feedback gains and thus getting the chance to better exploit the hardware capabilities?

As shown in (25), the effects of modeling errors in the estimated $\boldsymbol{F}^{\mathrm{ext}}$ are scaled by the same factor as for the PD gains. This, however, makes it difficult to observe and isolate the influence of erroneous $\boldsymbol{F}^{\mathrm{ext}}$ feedback through task errors in practice, as shown in Fig. 14, since the increased PD gains suppress a portion of the task errors contributed by the erroneous $\boldsymbol{F}^{\mathrm{ext}}$ feedback as well. Consequently, the effects of modeling errors in $\boldsymbol{F}^{\mathrm{ext}}$ can only, or at least most reliably, be validated using force-torque sensor data (i. e., the ground truth of $\boldsymbol{F}^{\mathrm{ext}}$). However, this is not possible on our hardware. Because an analysis of the effects of further modeling errors, such as those in the inertia matrix, lies beyond the scope of this article, we refer the reader to the relevant literature [58], [59].

While the validation parts (and particularly the 100.000 simulations in Section V-C) clearly indicate that the feedback scaling matrices feature lower elements if the natural inertia is preserved or naturally decoupled by FND, in contrast to inverse dynamics approaches, a mathematical proof for this hypothesis is difficult to find. Why does the full natural decoupling such as illustrated in Fig. 2 not cause similar problems as the full artificial decoupling although the closed-loop inertia matrix is also modified? In fact, there exists a physically intuitive explanation. The step from full natural coupling to full natural decoupling requires the annihilation of outer-blockdiagonal elements of the inertia matrix. These matrix elements are physically bounded, cf. the assumptions in Section II, and they represent well-defined power flows between the subsystems. The removal of those terms to obtain the block-diagonal structure of FND consequently requires well-defined and bounded control actions only. Actually, up to this point the same applies to inverse dynamics approaches as well. However, the difference arises in the subsequent step, where inverse dynamics additionally requires to remove the blockdiagonal elements and *add* artificial, constant terms instead. These new terms may require excessive control actions because they may not have any physical connection with the original system anymore. These terms may look unproblematic in the closed-loop dynamics but they potentially require excessively large feedback gains to install. In other words, the problems do not arise from the removal of natural terms but from the introduction of non-natural terms instead.

Regarding the passivity analysis, the approach presented here employs methods from passivity- and energy-based control [47], [49]. Consequently, it exploits similar features as the well-established IDA-PBC framework [39]. In particular, the beneficial property stated in Assumption 2 is used as well as the design choice to decouple the inertia matrix [40].

While the particular control law (25) provides beneficial properties in terms of stability and passivity, its superior features basically ground on the main principle of natural task-space decoupling. Consequently, it is expected that the adoption of this way to treat the closed-loop inertia is transferable to other control design methods straightforwardly. Among others, that might include MPC, numerical concepts utilizing QP formulations, or learning-based approaches. Irrespective of the chosen method, the enforcement of a closed-loop inertia will inevitably (and possibly implicitly) result in a scaling action such as shown in the third column of Table I. The presented results clearly indicate that choosing (19) combines the preferable full task-space decoupling from inverse dynamics with practically low effective feedback gains to be implemented in the lower-level control loops.

VIII. Conclusions and Future Work

A new multi-tasking control framework for kinematically redundant robots has been presented, which combined two fundamentally different features. First, the task-space dynamics of all subtasks could be fully dynamically decoupled such as known from classical inverse dynamics. Second, the superior practical robustness of passivity-based approaches has been adopted due to the application of low effective feedback gains. The provided theoretical analysis included proofs of stability and passivity and was then confirmed by simulations and comparative experiments.

In the future, the focus will be put on the improved feedback of external forces and torques. As discussed in Section VII, the quality of the respective estimations and measurements is often poor, which impedes its active feedback during highly dynamic motions. However, new hardware setups exploiting a redundant arrangement of sensors [60] have recently shown to be capable of solving this problem.

IX. Appendix

The following stability theorem is taken from [46, p. 147 and p. 154] to conduct the proof of stability in Section IV-A.

Theorem 1. *[46] Consider the non-autonomous system*

$$\dot{\boldsymbol{z}} = \boldsymbol{h}(t, \boldsymbol{z}) \tag{45}$$

where $\boldsymbol{h} : [0, \infty) \times Z \to \mathbb{R}^{2n}$ *is piecewise continuous in* t *and locally Lipschitz in* $\boldsymbol{z}$ *on* $[0, \infty) \times Z$*, and* $Z \subset \mathbb{R}^{2n}$ *is a domain that contains the origin* $\boldsymbol{z} = \boldsymbol{0}$*. Let* $\boldsymbol{z} = \boldsymbol{0}$ *be an equilibrium point for* (45) *and* $S : [0, \infty) \times Z \to \mathbb{R}$ *be a continuously differentiable function such that*

$$\alpha_1 ||\boldsymbol{z}||^\beta \leq S(t, \boldsymbol{z}) \leq \alpha_2 ||\boldsymbol{z}||^\beta \tag{46}$$

$$\frac{\partial S}{\partial t} + \frac{\partial S}{\partial \boldsymbol{z}} \boldsymbol{h}(t, \boldsymbol{z}) \leq -\alpha_3 ||\boldsymbol{z}||^\beta \tag{47}$$

$\forall\ t \geq 0$ *and* $\forall\ \boldsymbol{z} \in Z$*, where* $\alpha_1, \alpha_2, \alpha_3$*, and* β *are positive constants. Then* $\boldsymbol{z} = \boldsymbol{0}$ *is exponentially stable. If the assumptions hold globally, then* $\boldsymbol{z} = \boldsymbol{0}$ *is globally exponentially stable.*

TABLE V
QUALITATIVE COMPARISON OF THE DIFFERENT APPROACHES SKETCHED IN FIG. 2 WITH FIVE RATINGS (– –/–/**0**/+/+ +)

	Full natural coupling	**Hierarchical decoupling**	**Full natural decoupling**	**Full artificial decoupling**
Dynamic task decoupling	– –	+	+ +	+ +
Effective feedback gains	+ +	+	+	– –
Robustness due to F^{ext} feedback	+ +	+	+	– –
Behavior in singularities	+ (PD) , – (PD+)	– –	– –	– –
Theoretical convergence properties	–	**0**	+	+ +
Implementation examples	Task-space PD or PD+ [25]–[28]	Nullspace controllers [17]–[19], [31], [32]	FND control (25)	Inv. dynamics, computed torque [35, p. 429]

REFERENCES

[1] Y. Nakamura, H. Hanafusa, and T. Yoshikawa, "Task-Priority Based Redundancy Control of Robot Manipulators," *International Journal of Robotics Research*, vol. 6, no. 2, pp. 3–15, June 1987.

[2] J. H. Hollerbach and K. C. Suh, "Redundancy Resolution of Manipulators through Torque Optimization," *IEEE Journal of Robotics and Automation*, vol. RA-3, no. 4, pp. 308–316, August 1987.

[3] B. Siciliano and J.-J. Slotine, "A General Framework for Managing Multiple Tasks in Highly Redundant Robotic Systems," in *Proc. of the 5th International Conference on Advanced Robotics*, June 1991, pp. 1211–1216.

[4] O. Khatib, "A Unified Approach for Motion and Force Control of Robot Manipulators: The Operational Space Formulation," *IEEE Journal of Robotics and Automation*, vol. RA-3, no. 1, pp. 43–53, February 1987.

[5] L. Righetti, J. Buchli, M. Mistry, and S. Schaal, "Inverse Dynamics Control of Floating-Base Robots with External Constraints: a Unified View," in *Proc. of the 2011 IEEE International Conference on Robotics and Automation*, May 2011, pp. 1085–1090.

[6] O. Khatib, L. Sentis, J. Park, and J. Warren, "Whole-Body Dynamic Behavior and Control of Human-like Robots," *International Journal of Humanoid Robotics*, vol. 1, no. 1, pp. 29–43, March 2004.

[7] L. Sentis and O. Khatib, "Synthesis of Whole-Body Behaviors through Hierarchical Control of Behavioral Primitives," *International Journal of Humanoid Robotics*, vol. 2, no. 4, pp. 505–518, January 2005.

[8] L. Sentis, J. Park, and O. Khatib, "Compliant Control of Multicontact and Center-of-Mass Behavior in Humanoid Robots," *IEEE Transactions on Robotics*, vol. 26, no. 3, pp. 483–501, June 2010.

[9] M. Mistry, J. Buchli, and S. Schaal, "Inverse dynamics control of floating base systems using orthogonal decomposition," in *2010 IEEE international conference on robotics and automation*. IEEE, 2010, pp. 3406–3412.

[10] J. Moura, V. Ivan, M. S. Erden, and S. Vijayakumar, "Equivalence of the projected forward dynamics and the dynamically consistent inverse solution," in *Robotics: Science and Systems 2019*, 2019, pp. 1–10.

[11] N. Y. Lii *et al.*, "Introduction to Surface Avatar: the First Heterogeneous Robotic Team to be Commanded with Scalable Autonomy from the ISS," in *Proceedings of the International Astronautical Congress, IAC*. International Astronautical Federation, IAF, 2022.

[12] A. Escande, N. Mansard, and P.-B. Wieber, "Hierarchical quadratic programming: Fast online humanoid-robot motion generation," *International Journal of Robotics Research*, vol. 33, no. 7, pp. 1006–1028, June 2014.

[13] A. Herzog, N. Rotella, S. Mason, F. Grimminger, S. Schaal, and L. Righetti, "Momentum control with hierarchical inverse dynamics on a torque-controlled humanoid," *Autonomous Robots*, vol. 40, no. 3, pp. 473–491, March 2016.

[14] K. Bouyarmane and A. Kheddar, "On Weight-Prioritized Multitask Control of Humanoid Robots," *IEEE Transactions on Automatic Control*, vol. 63, no. 6, pp. 1632–1647, June 2018.

[15] E. M. Hoffman, A. Laurenzi, L. Muratore, N. G. Tsagarakis, and D. G. Caldwell, "Multi-Priority Cartesian Impedance Control Based on Quadratic Programming Optimization," in *2018 IEEE International Conference on Robotics and Automation (ICRA)*, 2018, pp. 309–315.

[16] J. D. M. Osorio and F. Allmendinger, "A Suitable Hierarchical Framework with Arbitrary Task Dimensions under Unilateral Constraints for physical Human Robot Interaction," in *2022 IEEE International Conference on Autonomous Robot Systems and Competitions (ICARSC)*, 2022, pp. 66–72.

[17] A. Karami, H. Sadeghian, M. Keshmiri, and G. Oriolo, "Hierarchical tracking task control in redundant manipulators with compliance control in the null-space," *Mechatronics*, vol. 55, pp. 171–179, November 2018.

[18] A. Dietrich and C. Ott, "Hierarchical Impedance-Based Tracking Control of Kinematically Redundant Robots," *IEEE Transactions on Robotics*, vol. 36, no. 1, pp. 204–221, February 2020.

[19] W. Sun, Y. Yuan, and H. Gao, "Hierarchical Control for Partially Feasible Tasks With Arbitrary Dimensions: Stability Analysis for the Tracking Case," *IEEE Transactions on Automatic Control*, 2024.

[20] J. Peters and S. Schaal, "Learning to control in operational space," *The International Journal of Robotics Research*, vol. 27, no. 2, pp. 197–212, 2008.

[21] D. Nicolis, F. Allevi, and P. Rocco, "Operational Space Model Predictive Sliding Mode Control for Redundant Manipulators," *IEEE Transactions on Robotics*, vol. 36, no. 4, pp. 1348–1355, 2020.

[22] J. Lee, S. H. Bang, E. Bakolas, and L. Sentis, "MPC-Based Hierarchical Task Space Control of Underactuated and Constrained Robots for Execution of Multiple Tasks," in *2020 59th IEEE Conference on Decision and Control (CDC)*, 2020, pp. 5942–5949.

[23] Y. Wang, Y. Liu, M. Leibold, M. Buss, and J. Lee, "Hierarchical Incremental MPC for Redundant Robots: a Robust and Singularity-Free Approach," *IEEE Transactions on Robotics*, vol. 40, pp. 2128–2148, 2024.

[24] B. Paden and R. Panja, "Globally asymptotically stable PD+ controller for robot manipulators," *International Journal of Control*, vol. 47, no. 6, pp. 1697–1712, 1988.

[25] F. L. Moro, M. Gienger, A. Goswami, N. G. Tsagarakis, and D. G. Caldwell, "An Attractor-based Whole-Body Motion Control (WBMC) System for Humanoid Robots," in *Proc. of the 13th IEEE-RAS International Conference on Humanoid Robots*, October 2013, pp. 42–49.

[26] J. Hermus, J. Lachner, D. Verdi, and N. Hogan, "Exploiting Redundancy to Facilitate Physical Interaction," *IEEE Transactions on Robotics*, vol. 38, no. 1, pp. 599–615, February 2022.

[27] C. Tiseo, W. Merkt, W. Wolfslag, S. Vijayakumar, and M. Mistry, "Safe and compliant control of redundant robots using superimposition of passive task-space controllers," *Nonlinear Dynamics*, vol. 112, pp. 1023–1038, 2024.

[28] R. Wen, Q. Rouxel, M. Mistry, Z. Li, and C. Tiseo, "Collaborative bimanual manipulation using optimal motion adaptation and interaction control: Retargeting human commands to feasible robot control references," *IEEE Robotics & Automation Magazine*, vol. 31, no. 4, pp. 68–80, 2023.

[29] C. Tiseo, W. Merkt, K. K. Babarahmati, W. Wolfslag, I. Havoutis, S. Vijayakumar, and M. Mistry, "Hapfic: An adaptive force/position controller for safe environment interaction in articulated systems," *IEEE Transactions on Neural Systems and Rehabilitation Engineering*, vol. 29, pp. 1432–1440, 2021.

[30] A. Dietrich, C. Ott, and A. Albu-Schäffer, "An overview of null space projections for redundant, torque-controlled robots," *International Journal of Robotics Research*, vol. 34, no. 11, pp. 1385–1400, Sept. 2015.

[31] B. K. Sæbϕ, K. Y. Pettersen, and J. T. Gravdahl, "Robust task-priority impedance control for vehicle-manipulator systems," in *2022 IEEE Conference on Control Technology and Applications (CCTA)*. IEEE, 2022, pp. 363–370.

[32] Y. Yuan and W. Sun, "Continuously Shaping Prioritized Jacobian Approach for Hierarchical Optimal Control with Task Priority Transition," *IEEE Transactions on Robotics*, pp. 1–18, February 2025.
[33] M. D. Fiore, G. Meli, A. Ziese, B. Siciliano, and C. Natale, "A general framework for hierarchical redundancy resolution under arbitrary constraints," *IEEE Transactions on Robotics*, vol. 39, no. 3, pp. 2468–2487, June 2023.
[34] W. Sun and Y. Yuan, "Passivity based hierarchical multi-task tracking control for redundant manipulators with uncertainties," *Automatica*, vol. 155, p. 111159, 2023.
[35] K. M. Lynch and F. C. Park, *Modern Robotics: Mechanics, Planning, and Control*. Cambridge University Press, 2017.
[36] O. Khatib, M. Jorda, J. Park, L. Sentis, and S.-Y. Chung, "Constraint-consistent task-oriented whole-body robot formulation: Task, posture, constraints, multiple contacts, and balance," *The International Journal of Robotics Research*, vol. 41, no. 13-14, pp. 1079–1098, 2022.
[37] A. Dietrich, X. Wu, K. Bussmann, M. Harder, M. Iskandar, J. Englsberger, C. Ott, and A. Albu-Schäffer, "Practical consequences of inertia shaping for interaction and tracking in robot control," *Control Engineering Practice*, vol. 114, p. 104875, 2021.
[38] J. Englsberger, A. Dietrich, G.-A. Mesesan, G. Garofalo, C. Ott, and A. Albu-Schäffer, "MPTC - Modular Passive Tracking Controller for Stack of Tasks Based Control Frameworks," *16th Robotics: Science and Systems, RSS 2020*, 2020.
[39] R. Ortega, A. Van Der Schaft, B. Maschke, and G. Escobar, "Interconnection and damping assignment passivity-based control of port-controlled Hamiltonian systems," *Automatica*, vol. 38, no. 4, pp. 585–596, 2002.
[40] F. Valentinis, T. Battista, and C. Woolsey, "A maneuvering model for an underwater vehicle near a free surface-Part III: Simulation and control under waves," *IEEE Journal of Oceanic Engineering*, vol. 48, no. 3, pp. 752–777, 2023.
[41] F. Ghorbel, B. Srinivasan, and M. W. Spong, "On the uniform boundedness of the inertia matrix of serial robot manipulators," *Journal of Robotic Systems*, vol. 15, no. 1, pp. 17–28, 1998.
[42] R. Gunawardana and F. Ghorbel, "On the uniform boundedness of the coriolis/centrifugal terms in the robot equations of motion," *International Journal of Robotics and Automation*, vol. 14, no. 52, pp. 45–53, 1999.
[43] R. M. Murray, Z. Li, and S. S. Sastry, *A Mathematical Introduction to Robotic Manipulation*. CRC Press, 1994.
[44] X. Wu, C. Ott, A. Albu-Schäffer, and A. Dietrich, "Passive decoupled multitask controller for redundant robots," *IEEE Transactions on Control Systems Technology*, vol. 31, no. 1, pp. 1–16, 2022.
[45] J.-J. E. Slotine, W. Li *et al.*, *Applied nonlinear control*. Prentice hall Englewood Cliffs, NJ, 1991, vol. 199, no. 1.
[46] H. K. Khalil, *Nonlinear Systems (Third Edition)*. Prentice Hall, 2002.
[47] A. van der Schaft, *L2-Gain and Passivity Techniques in Nonlinear Control*, 3rd ed. Springer International Publishing, 2017.
[48] W. Borutzky, *Bond graphs for modelling, control and fault diagnosis of engineering systems*. Springer, 2017.
[49] S. Stramigioli, "Energy-Aware Robotics," in *Mathematical Control Theory I*, ser. Lecture Notes in Control and Information Sciences 461, M. K. Camlibel, A. A. Julius, R. Pasumarthy, and J. M. A. Scherpen, Eds. Springer International Publishing Switzerland, 2015, ch. 3, pp. 37–50.
[50] J. Lee, N. Mansard, and J. Park, "Intermediate Desired Value Approach for Task Transition of Robots in Kinematic Control," *IEEE Transactions on Robotics*, vol. 28, no. 6, pp. 1260–1277, December 2012.
[51] A. Dietrich, A. Albu-Schäffer, and G. Hirzinger, "On Continuous Null Space Projections for Torque-Based, Hierarchical, Multi-Objective Manipulation," in *Proc. of the 2012 IEEE International Conference on Robotics and Automation*, May 2012, pp. 2978–2985.
[52] N. Dehio, D. Kubus, and J. J. Steil, "Continuously shaping projections and operational space tasks," in *2018 IEEE/RSJ International Conference on Intelligent Robots and Systems (IROS)*. IEEE, 2018, pp. 5995–6002.
[53] D. Di Vito, C. Natale, and G. Antonelli, "A Comparison of Damped Least Squares Algorithms for Inverse Kinematics of Robot Manipulators," *IFAC-PapersOnLine*, vol. 50, no. 1, pp. 6869–6874, 2017, 20th IFAC World Congress.
[54] X. Wu, A. Albu-Schäffer, and A. Dietrich, "Singularity-Robust Prioritized Whole-Body Tracking and Interaction Control with Smooth Task Transitions," in *Proc. of the 2024 IEEE International Conference on Robotics and Automation*, May 2024.
[55] A. De Luca and R. Mattone, "Actuator failure detection and isolation using generalized momenta," in *2003 IEEE International Conference on Robotics and Automation*, vol. 1, Sep. 2003, pp. 634–639.
[56] A. De Luca, A. Albu-Schäffer, S. Haddadin, and G. Hirzinger, "Collision Detection and Safe Reaction with the DLR-III Lightweight Manipulator Arm," in *Proc. of the 2006 IEEE/RSJ International Conference on Intelligent Robots and Systems*, October 2006, pp. 1623–1630.
[57] W. Tang, W. Wang, and S. Wang, "Partially decoupled impedance motion force control using prioritized inertia shaping," *IEEE Robotics and Automation Letters*, vol. 9, no. 9, pp. 7621–7628, September 2024.
[58] J. Nakanishi, R. Cory, M. Mistry, J. Peters, and S. Schaal, "Operational Space Control: A Theoretical and Empirical Comparison," *International Journal of Robotics Research*, vol. 27, no. 6, pp. 737–757, June 2008.
[59] P. Di Lillo, G. Antonelli, and C. Natale, "Effects of dynamic model errors in task-priority operational space control," *Robotica*, vol. 39, no. 9, pp. 1642–1653, 2021.
[60] M. Iskandar, A. Albu-Schäffer, and A. Dietrich, "Intrinsic sense of touch for intuitive physical human-robot interaction," *Science Robotics*, vol. 9, no. 93, p. eadn4008, 2024.

Alexander Dietrich received the Dr.-Ing. degree from the Technical University of Munich (TUM), Germany, in 2015. He joined the Institute of Robotics and Mechatronics of the German Aerospace Center (DLR) in 2010 and has led the Whole-Body Control Group since 2017. He received the Georges Giralt PhD Award for the best European doctoral thesis in robotics in 2016 and the DLR Science Award in 2020. He has served as editor of IEEE ICRA, associate editor of IEEE RA-L, IEEE RA-M, and IEEE T-RO, and as co-chair of the IEEE RAS Technical Committee on Whole-Body Control. Since 2019 he has lectured at TUM on robot control. His research interests include control, stability theory, humanoid robotics, mobile manipulation, and safe physical human-robot interaction.

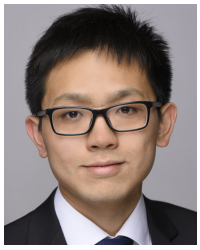

Xuwei Wu received the B.E. degree in vehicle engineering from the Tongji University, Shanghai, China, in 2013, and the M.Sc. degree in mechanical engineering from the Technical University of Munich (TUM), Germany, in 2016. In 2019, he joined the German Aerospace Center (DLR), Institute of Robotics and Mechatronics, as a research assistant. His current research interests include nonlinear stability theory, whole-body control of humanoid robots, and safe physical human-robot interaction.

Maged Iskandar received a master's degree in mechatronics with a focus on system dynamics and robotics from the Politecnico di Torino in 2017. He is currently a research scientist at the DLR Institute of Robotics and Mechatronics. His research interests include impedance and force control, whole-body control, and human-robot interaction.

Alin Albu-Schäffer received his M.S. in electrical engineering from the Technical University of Timisoara, Romania in 1993 and his Ph.D. in automatic control from the Technical University of Munich in 2002. Since 2012 he is the head of the Institute of Robotics and Mechatronics at the German Aerospace Center (DLR). Moreover, he is a professor at the Technical University of Munich, holding the Chair for "Sensor-Based Robotic Systems and Intelligent Assistance Systems" at the School of Computation, Information and Technology. His personal research interests include robot design, modeling and control, nonlinear control, flexible-joint and variable compliance robots, impedance and force control, physical human-robot interaction, bio-inspired robot design and control. He received several awards, including the IEEE King-Sun Fu Best Paper Award of the Transactions on Robotics in 2012 and 2014; several ICRA and IROS Best Paper Awards as well as the DLR Science Award. He was strongly involved in the development of the DLR light-weight robot and its commercialization through technology transfer to KUKA. He is the coordinator of euROBIN, the European network of excellence on intelligent robotics, IEEE Fellow and RAS-AdCom member.

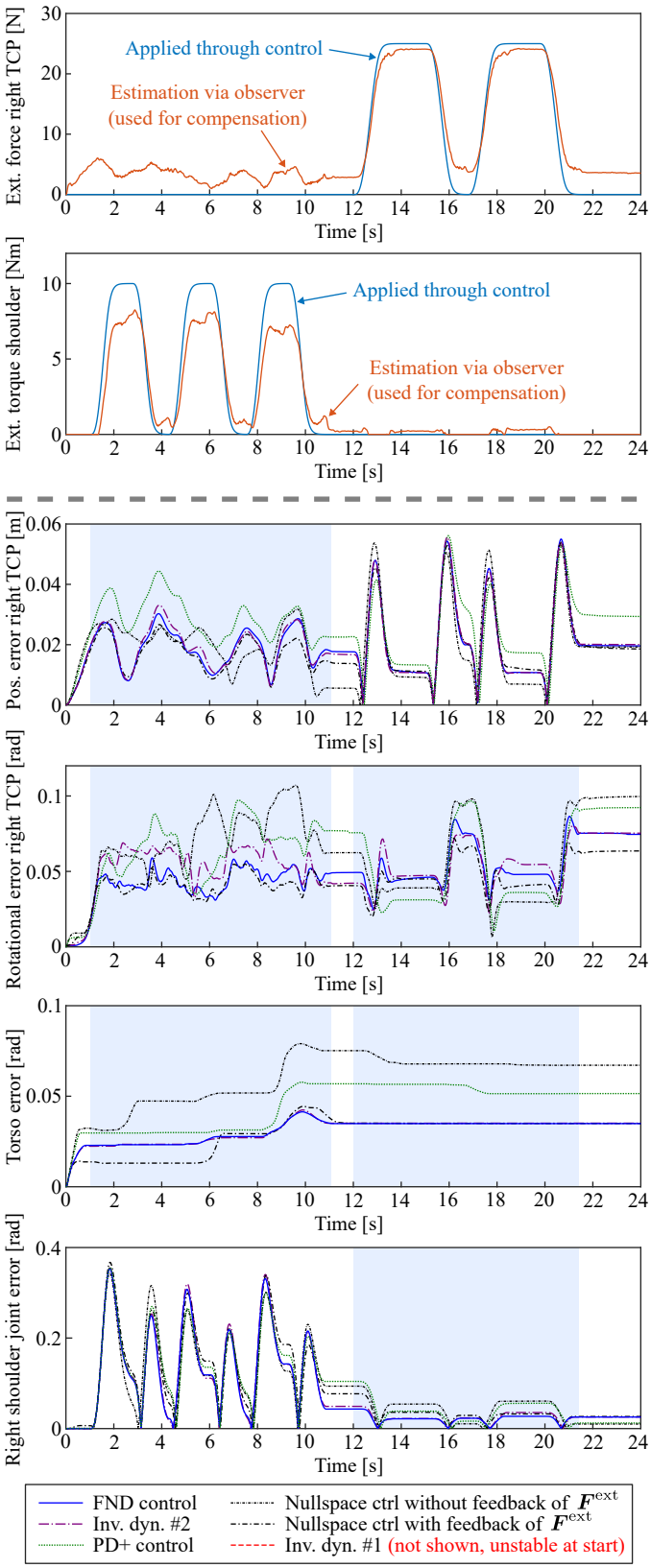

Fig. 14. Experiment #2: Effect of external interactions on the task spaces. Inverse dynamics #1 is not shown since it causes instability immediately.